Master thesis

CERN Technical Students Programme
1 June 2011 – 30 April 2012

Interactions of Particles with Momenta of 1–10 GeV in a Highly Granular Hadronic Calorimeter with Tungsten Absorbers

Ching Bon Lam

Applied Physics Master
Faculteit Technische Natuurwetenschappen
Universiteit Twente

Supervised by
Dr. Angela Lucaci-Timoce, CERN
Prof. dr. ing. Bob van Eijk, Nikhef / Universiteit Twente

Abstract

Linear electron-positron colliders are proposed to complement and extend the physics programme of the Large Hadron Collider at CERN. In order to satisfy the physics goal requirements at linear colliders, detector concepts based on the Particle Flow approach are developed. Central to this approach are a high resolution tracker and a highly granular calorimeter which provide excellent jet energy resolution and background separation.

The Compact Linear Collider (CLIC) is an electron-positron collider under study, aiming at centre-of-mass energies up to 3 TeV. For the barrel hadronic calorimeter of experiments at CLIC, a detector with tungsten absorber plates is considered, as it is able to contain shower jets while keeping the diameter of the surrounding solenoid magnet limited.

A highly granular analogue hadron calorimeter with tungsten absorbers was built by the CALICE collaboration. This thesis presents the analysis of the low-momentum data ($1\,\text{GeV} \leq p \leq 10\,\text{GeV}$) recorded in 2010 at the CERN Proton Synchrotron (PS).

The energy resolution is measured for electrons, pions and protons, and is compared with the performance of other calorimeters. In addition, comparisons of data with Monte Carlo are done for hadronic shower shapes, in order to validate GEANT4 simulation models of the development of hadronic showers in tungsten.

The electromagnetic resolution for a tungsten based HCAL is worse than for an iron based HCAL. This is expected due to the shorter radiation length of tungsten.

The shower maximum t_{max} for electrons is between 3.9 X_0 and 5.6 X_0. The mean shower radius has a maximum value of 62 mm at 1 GeV and decreases to 26 mm at 6 GeV. The mean shower radius for protons is between 74 mm and 81 mm, while for the pions they are between 69 mm and 78 mm.

Three physics lists were studied to validate the hadron interactions in tungsten: QGSP_BERT_HP, FTFP_BERT_HP and QGSP_BIC_HP. In general the Monte Carlo is within 8% agreement with the data.

Contents

1 Introduction

The Standard Model

Since the discovery of the electron (1897) by J.J. Thompson, more particles have been discovered such as the proton (1919), neutron (1932), positron (1932) and the muon (1937). By the early of 1960s hundreds of new particles and their excitations have been observed. A model of the underlying structure has been developed by studying the properties of the particles and their interactions. It is called the Standard Model (SM) of particle physics [1].

According to the Standard Model, a total of 12 fermion particles makes up for all matter: six quarks and six leptons. The interactions between them are mediated by boson particles: electromagnetism between charged particles by the photon, the weak force between all fermions by the W and the Z, and the strong force between quarks by the gluon. Gravitational interaction, however, is not included in the Standard Model.

The Standard Model has succesfully explained experimental results and precisely predicted phenomena. Nevertheless, there are still open questions such as:

- To unify the weak and the electromagnetic force mathematically, particles have to be massless. However, it is observed that particles do have mass. The Standard Model postulates the Higgs mechanism [2] where particles acquire mass by interacting with the Higgs field*. A goal of the current and future experiments is to investigate the mass generation and the electroweak symmetry breaking.

- Antimatter is discovered around 1930. Assuming the universe started with a balanced amount of antimatter and matter, the question is why the current world predominantly consists of matter (baryon asymmetry). It has been observed that matter and antimatter does not behave exactly the same (violation of charge conjugation and parity symmetry) but further study is required.

*The Higgs mechanism can be seen as a method to add mass terms to the Lagrangian such that it is gauge invariant at the cost of adding a scalar field.

Experiments

A collider experiment in particle physics involves an accelerator of particles and a detector for the measurement of the particle collisions. The choice between using a lepton beam or hadron beam depends on the research goals; each have their advantages and disadvantages. In general hadron colliders are built for discovery while lepton colliders are built to do precise measurements. However, each have different production rates of and access to physics processes which makes the one preferable over the other depending on the type of the measurement. Lepton and hadron colliders are thus complementary tools for studying particle physics.

The Large Hadron Collider (LHC) at CERN[†] is built to search for and explore new physics such as the Higgs boson and supersymmetry (SUSY) while it also allows for measurement of the CP violation in B-meson decays and study of the quark-gluon plasma through heavy ion collisions. High energy e^- e^+ colliders have been proposed to complement and to extend the LHC physics programme [3]: the International Linear Collider (ILC [4]) and the Compact Linear Collider (CLIC [5]). Besides allowing precision measurements of new physics uncovered at the LHC, they give access to additional physics processes and thus provides new discovery potential.

Accelerators

Both ILC and CLIC are linear colliders (LC) as opposed to the LHC, a circular collider. In a circular collider particles are accelerated by the same accelerator structures in the ring every turn. The size is therefore smaller than a linear collider of comparable power. The maximum energy for electrons in a ring accelerator is however limited by synchrotron radiation due to its small mass. This effect is absent in linear colliders and they are currently the only cost-effective way to accelerate electrons to the scale of TeV.

Interesting physics processes are likely to be rare. A high luminosity (collision rate) is therefore a driving factor in the design of a collider. The beam repetition rate is inherently lower at a linear collider than a circular collider (for example 40 MHz at LHC vs. 50 Hz at CLIC). Thus, to achieve a high luminosity at an LC a smaller spot size is required. This results however in strong electromagnetic radiation (beamstrahlung) caused by the opposite beams interacting with each other. It dilutes the luminosity spectrum while large background is created.

Detector

The detector performance requirements at CLIC are determined by the precision of the physics goals. The principal factors driving the overall design of a detector at CLIC are the requirement of excellent jet energy resolution and the need to identify and reject calorimeter energy depositions from beam-induced background.

Detector concepts based on the Particle Flow approach [6] are in development to satisfy the requirements. In this approach a high resolution tracker is used for determining the energy of charged particles while the highly granular calorimeter has the same function but for neutral particles. In addition, the high granularity of

[†]European Organization for Nuclear Research. It was originally called *Conseil Européen pour la Recherche Nucléaire*. The acronym CERN has been kept after the name change.

the calorimeter makes it possible to distinguish particles within jets. The combined information allows to separate W from Z boson decays on an event-by-event basis.

A calorimeter with tungsten aborbers is considered for the barrel region. Tungsten is a dense material and allows a more compact calorimeter than when iron is used as the absorber. This is important for the barrel region as it limits the diameter of the surrounding solenoid magnet and thus the detector cost. In addition, energy depositions in tungsten are more localized, leading to less confusion in identifying particles.

A highly granular analogue hadron calorimeter with tungsten absorbers (W-HCAL) has been developed by the CALICE[‡] collaboration. The W-AHCAL was tested in several test beam campaigns at CERN in 2010 and 2011. This thesis presents the analysis of the low-momentum ($p \leq 10\,\mathrm{GeV}$[§]) data taken at the Proton Synchrotron (PS) test beam at CERN in 2010. There is no extensive data neither on tungsten nor on hadronic shapes. This analysis is intended to provide data for the validation of hadronic simulation models for tungsten, including the shower shapes. In addition, the energy resolution is measured for electrons, pions and protons to compare its performance with other calorimeters.

The outline of the thesis is as follows. The basic concepts in calorimetry are discussed in chapter 2. The prototype detector and its calibration is described in chapter 3, along with the description of the test beam setup. An overview of the analysis chain is given in chapter 4. It is then followed by the actual analysis of the data: chapter 5 for e^+/e^- and chapter 6 for the hadrons.

[‡]Calorimetry at Linear Collider Experiments

[§]In this thesis the natural system with $\hbar = c = 1$ is used.

2 Calorimetry

This chapter starts with a description of what calorimetry is. It continues with two sections which will discuss the following topics in more detail: the interaction of particles with matter in section 2.1 and the energy resolution in section 2.2.

Calorimetry in high energy physics concerns the measurement of the energy of particles through absorption. The energy of the incident particle is proportional to the measured response of the calorimeter. The particle is usually captured in dense material and loses all its energy.

There are two types of calorimeters: *homogeneous* and *sampling*. In a homogeneous calorimeter, the whole detector volume is sensitive. In a sampling calorimeter, however, there is an additional absorber material in front of the sensitive part. Such a device consists of multiple layers of alternating absorber and sensitive material.

A calorimeter is called compensating when the response to electrons is the same as the response to pions:

$$e/\pi = 1 \tag{2.1}$$

A non-compensating calorimeter ($e/\pi \neq 1$) has a non-linear response to the particle's energy. This is because the electromagnetic fraction of pion-induced showers increases with energy [7].

2.1. Interaction of particles with matter

Particles interact with matter in different ways depending on their type and properties. Electrically charged particles (such as electrons, muons and protons) interact with each other via the electromagnetic force. Photons are neutral massless fundamental particles that couple to electrically charged particles only. Hadrons are composite particles which can be either neutral or electrically charged. Charged hadrons also interact electromagnetically, however the strong interaction is the dominant force for all hadrons.

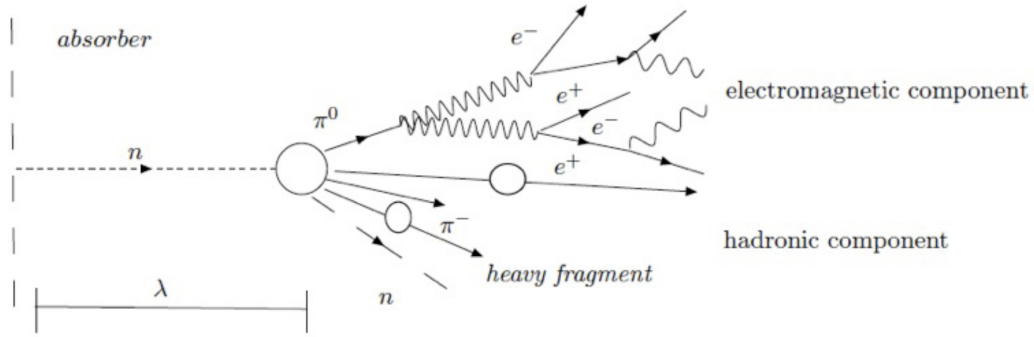

Figure 2.1.: A schematic representation of an interaction of a neutron with an absorber.

Table 2.1.: Characteristic lengths for iron and tungsten [8].

Material	λ_I [cm]	X_0[cm]	λ_I/X_0
Iron (Fe)	16.77	1.76	9.5
Tungsten (W)	9.95	0.35	28.4

A schematic representation of an interaction of a neutron with a nucleus is shown in Figure 2.1. The distance λ_I is called the *nuclear interaction length*. It is the mean distance before a hadronic particle undergoes an inelastic nuclear interaction. The electromagnetic counterpart is the *radiation length* X_0. It is the mean distance over which an electron loses all but $1/e$ of its energy by Bremsstrahlung.

The nuclear interaction length and the radiation length for iron and tungsten are shown in Table 2.1. The nuclear interaction length for tungsten is 41% shorter than iron, while the radiation length is 80% shorter. Calorimeters using tungsten can therefore be smaller.

The neutron interacts via the strong force with the nucleus and results into new hadrons (Figure 2.1). Pions are the lightest hadrons (around 140 MeV) and as a consequence they are abundantly produced. There are two charged pions, π^+ and π^- while there is only one neutral pion, π^0. A neutral pion decays into two photons (99% branching fraction [1]) or a photon and an e^- e^+ pair (1% branching fraction). The photons and electrons cascade further into an electromagnetic shower. Therefore, approximately one third of the energy in a hadronic shower is deposited through electromagnetic interactions. At energies in the order of the mass of the pion this approximation is not valid anymore as charged pions are created in pairs.

The energy loss of a muon in a scintillator (polystyrene) is shown in Figure 2.2. The critical energy ϵ_c is the energy where the loss due to radiative processes is equal to the loss due to ionization. Radiative processes include Bremsstrahlung, pair production and photo-nuclear interactions. The mean rate of energy loss for charged heavy particles (including muons but excluding electrons) is well described by the Bethe equation [1]:

$$-\left\langle \frac{\mathrm{d}E}{\mathrm{d}x} \right\rangle = K z^2 \frac{Z}{A} \frac{1}{\beta^2} \left[\frac{1}{2} \ln \frac{2 m_e c^2 \beta^2 \gamma^2 T_\mathrm{max}}{I} - \beta^2 - \frac{\delta(\beta\gamma)}{2} \right] \tag{2.2}$$

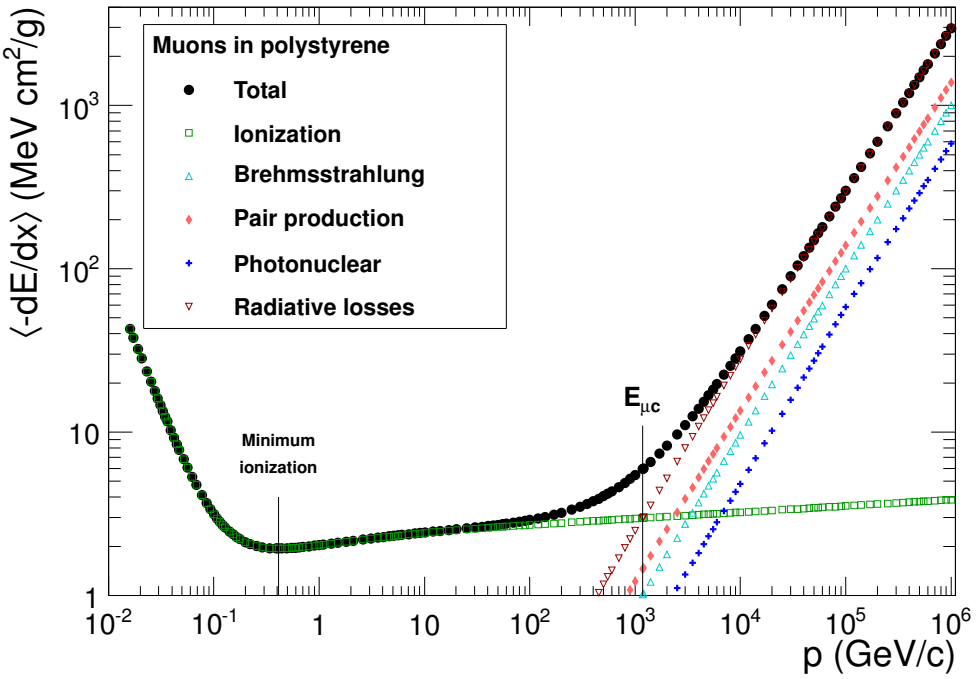

Figure 2.2.: The average energy loss of muons in polystyrene. Compiled from [8].

The muon is used for calibration (section 3.2). Between the energies 0.2 and 300 GeV the energy loss is approximately constant. The detector response to muons is therefore expected to be constant from the front to the end of the calorimeter.

Particles with the mean energy loss rates close to the minimum are said to be minimum ionizing particles (MIPs) [1]. Muons are therefore in this case MIPs.

Protons and neutrons are released from the nucleus by spallation and evaporation. Only a small fraction of this energy will appear as a calorimeter response. Moreover, large event-to-event fluctuations can occur for the hadronic response. Other processes that do not result in an observable signal include backscattering and leakage due to muons, charged pions, neutrinos or slow neutrons.

2.2. Energy resolution

The detector response has large event-to-event fluctuations due to processes that do not result in an observable signal and thus do not contribute in the detector response. Consequently, there is a spread in the detector response for particles with the same energy. The measurement of a particle's energy is therefore a statistical process.

An example of the energy distribution is shown in Figure 2.3. The mean of this distribution is a measure for the energy and the width a measure for the resolution.

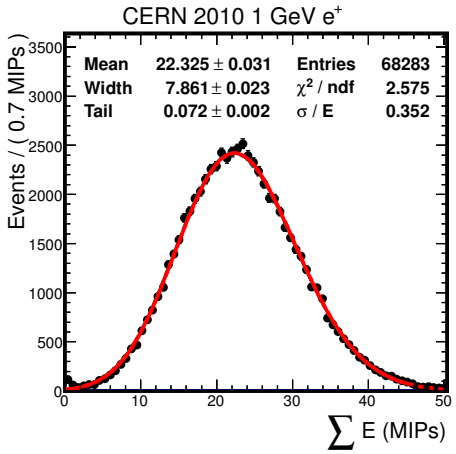

Figure 2.3.: Energy sum distribution of 1 GeV positrons. The response curve is fitted (red solid line) with the Novosibirsk function (Eq. 5.2).

The relative energy resolution is then defined as

$$\frac{\sigma_E}{E} = \frac{c_{\text{stochastic}}}{\sqrt{E}} \oplus \frac{c_{\text{noise}}}{E} \oplus c_{\text{constant}} \tag{2.3}$$

where E is the mean and σ_E the width of the distribution. The contributions to the energy resolution are: the stochastic term $c_{\text{stochastic}}$ due to Poisson statistics of the shower process; the electronic noise term c_{noise}; and the energy independent term c_{constant}.

For contributions that are mutually uncorrelated, they can be added in quadrature:

$$c_{total} = c_1 \oplus c_2 \oplus c_3 \tag{2.4}$$

$$= \sqrt{(c_1)^2 + (c_2)^2 + (c_3)^2} \tag{2.5}$$

When this is not the case, the contributions have to be added taking into account the correlations.

Energy resolutions for various electromagnetic calorimeters are listed in Table 2.2. Table 2.3 gives an overview of the resolution of hadronic calorimeters.

Table 2.2.: Energy resolutions of electromagnetic sampling calorimeters in various experiments [9, 10].

	ECAL	
Experiment	Material	Resolution
ATLAS	Lead, LAr	$\frac{10\%}{\sqrt{E\,(\mathrm{GeV})}} \oplus \frac{0.170}{E\,(\mathrm{GeV})} \oplus 0.7\%$
CMS	$PbWO_4$	$\frac{2.8\%}{\sqrt{E\,(\mathrm{GeV})}} \oplus \frac{0.125}{E\,(\mathrm{GeV})} \oplus 0.3\%$
LHCb	Lead, scintillator	$\frac{10\%}{\sqrt{E\,(\mathrm{GeV})}} \oplus 1\%$
ALICE	$PbWO_4$	$\frac{3.3\%}{\sqrt{E\,(\mathrm{GeV})}} \oplus \frac{0.18}{E\,(\mathrm{GeV})} \oplus 1.1\%$

Table 2.3.: Energy resolutions of hadronic sampling calorimeters in various experiments [9, 10].

	HCAL	
Experiment	Material	Resolution
ATLAS	Steel, scintillator	$\frac{52.9\%}{\sqrt{E\,(\mathrm{GeV})}} \oplus 5.7\%$
LHCb	Iron, scintillator	$\frac{(69\pm5)\%}{\sqrt{E\,(\mathrm{GeV})}} \oplus (9 \pm 2)\,\%$

3
CERN 2010 test beam

In 2010 there were two test beam periods with the W-AHCAL at the CERN proton synchrotron (PS). The study of the test beam data has several purposes:

1. Validation of hadronic simulation models in tungsten. This include data on hadron shower shapes thanks to the high granularity of the detector.

2. The measurement of the energy resolution of the detector.

The beam momentum is between 1 GeV and 10 GeV and the beam consists of mainly electrons, muons, pions and protons (section 3.4.5).

This chapter starts with the description of the calorimeter prototype and its calibration procedure in section 3.1 and section 3.2, respectively. Then the beam line setup is presented in section 3.3. Finally, the particle identification is discussed in section 3.4. This includes the determination of the beam composition.

3.1. Tungsten analogue hadronic calorimeter prototype

The W-AHCAL prototype in 2010 was a 1 m^3 detector consisting of 30 layers. Each layer has a tungsten absorber, scintillator as active material, and various materials for the support structure. A layer as implemented in the simulation [11] is shown in Figure 3.1. For the dimensions of each element see Table 3.1.

The active layer is divided in tiles of different sizes (Figure 3.2). The core consists of 10×10 tiles of 3×3 cm^2 arranged in a square. It is surrounded by tiles of 6×6 cm^2 and tiles of 12×12 cm^2. With 216 tiles in each layer and 30 layers in the prototype, there are a total of 6480 tiles.

Each scintillating tile has a wavelength-shifting (WLS) fiber that is inserted into a groove and is coupled to a Silicon Photomultiplier (SiPM, [14]) on one end via an air gap. The other fiber end is covered with a mirror to increase the light yield.

A SiPM consists of an array of avalanche photodiode (APD) pixels, operating in Geiger mode.

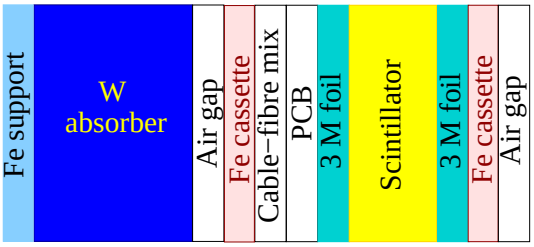

Figure 3.1.: A W-AHCAL layer as implemented in simulation [11].

Table 3.1.: Dimensions of the elements of an W-AHCAL layer [11] where the radiation length X_0 and interaction length λ_I are the values from GEANT4 [12].

	Thickness [mm]	X_0 [cm]	λ_I [cm]
Steel support	0.5	1.76	16.97
W absorber	10	0.39	10.81
Air gap	2×1.25	30392.1	71013.7
Steel cassette	2×2	1.76	16.97
3M foil	2×0.115	41.12	68.51
PCB	1	17.51	48.39
Cable-fiber mix	1.5	224.37	729.83
Scintillator	5	41.31	68.84
Total	24.73		

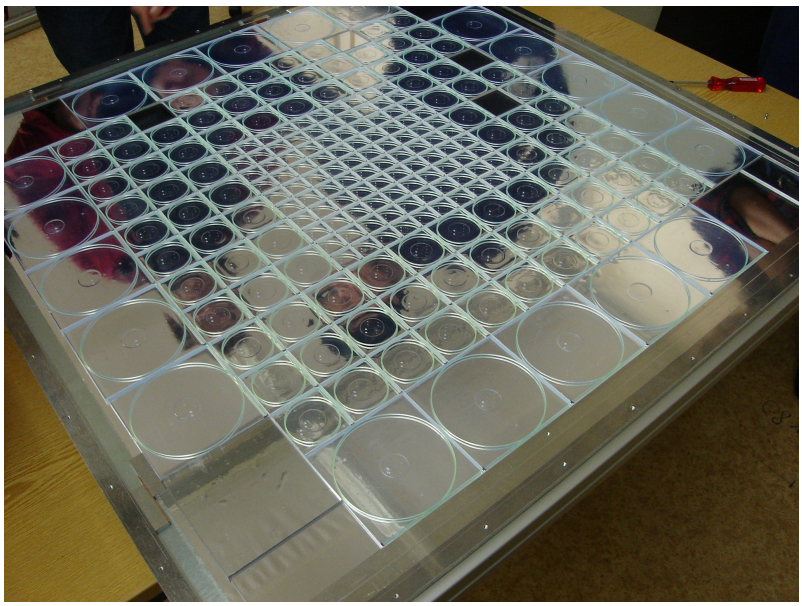

Figure 3.2.: Active material of an AHCAL layer divided in cells of different sizes [13].

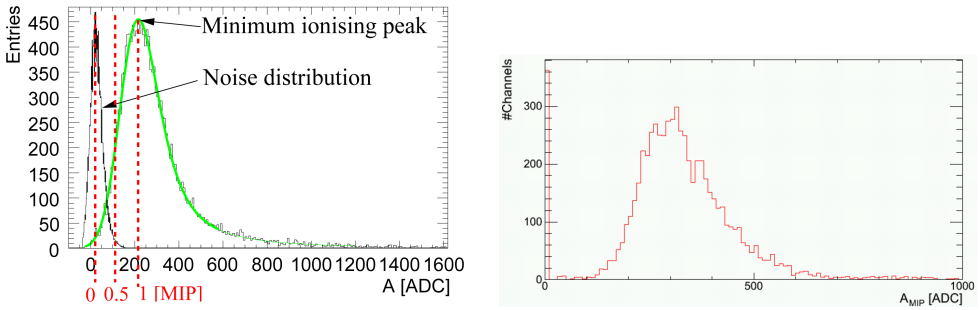

(a) (b) MIP values.

Figure 3.3.: (a) The cell response to a muon [15]. The ADC count value at the peak is defined as 1 MIP. (b) The distribution of the MIP values.

3.2. Calibration

The detector response is expressed in ADC counts while the energy of the particles is expressed in MIPs. Calibration is the procedure to establish a relationship between the two.

The calibration for this prototype consists of four parts. First, the pedestal level is subtracted from the cell response. Second, correction for the non-linear response of the SiPM is applied. Next, it is normalized to the MIP level. As the SiPM response depends on the temperature, correction for this is applied in the last step.

3.2.1. Single cell calibration

The following equation is used for single cell calibration:

$$E_i[\text{MIP}] \quad = \quad \frac{f_i^{-1}\left(A_i[\text{ADC}] - P_i[\text{ADC}]\right)}{M_i[\text{ADC/MIP}]} \tag{3.1}$$

where for each cell i the cell response is A_i, the pedestal P_i, and the MIP constant M_i. The function f_i^{-1} is to correct for the non-linear response of the SiPM and is discussed in section 3.2.2.

For beam events, each cell response A_i is subtracted with its pedestal baseline P_i, which is due to the ADC offset, cabling and grounding. In addition, there are fluctuations around the baseline due to electronic noise. These are measured during data acquisition with a random trigger.

Muons are used as minimum ionizing particles for the MIP calibration. An example of a cell response to a muon is shown in Figure 3.3.a. The spectrum is fitted with a Landau convoluted with a Gaussian. The most probable value of the fit is then defined as 1 MIP for the single cell.

3.2.2. SiPM response

There are two operational modes: physics mode and calibration mode. Physics mode uses a lower gain for increased dynamical range. This is used for data acquisition. Calibration mode, however, uses a special high gain, low noise mode to be able to resolve the single pixel spectrum.

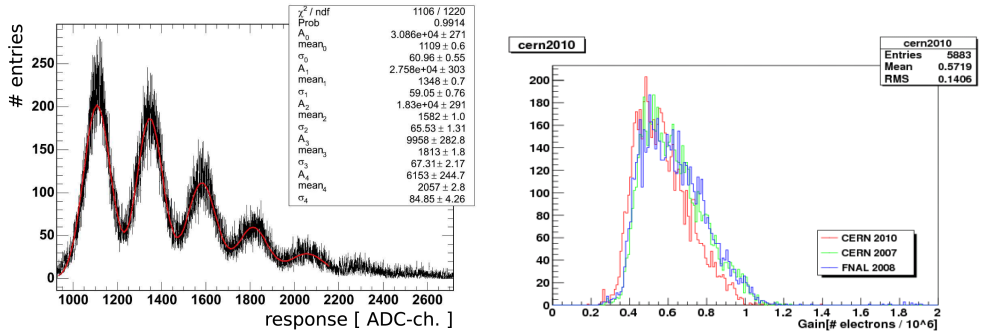

(a) (b)

Figure 3.4.: (a) A single gain calibration spectrum [16]. (b) The distribution of the gain values.

The non-linear response of the SiPM [16] is corrected by using:

$$f_i^{-1}\left(x_i\ [\mathrm{ADC}]\right) \quad = \quad \left[f^{-1}_{\mathrm{response},i}\left(\frac{x_i\ [\mathrm{ADC}]}{g_{\mathrm{PM},i}\ [\mathrm{ADC/pixel}]}\right)\right] \cdot g_{\mathrm{PM},i}\ [\mathrm{ADC/pixel}] \tag{3.2}$$

where for each cell i the input is $x_i = A_i - P_i$ and the gain constant $g_{\mathrm{PM},i}$ in physics mode. The gain is defined as the size of the charge signal of a single firing pixel.

An LED system is used for measuring the response of the tiles to different light intensities. An example spectrum in calibration mode is shown in Figure 3.4. A multi-Gaussian fit is used to determine the peaks. The distance between two peaks is one pixel and therefore the gain constant.

The gain constant is measured in calibration mode. To use it in physics mode, it is scaled by the inter-calibration factor

$$IC_i \quad = \quad \frac{PM_i}{CM_i} \tag{3.3}$$

This is the ratio of measurements for different light intensities in both physics and calibration mode.

A SiPM has a limited number of pixels. Also, the dead time is such that the pixel cannot activate more than once per event. An example for the therefore non-linear response function $f_{\mathrm{response},i}$ of a SiPM is shown in Figure 3.5 [16]. The correction function is the inverse of the response function and is given by

$$f^{-1}_{\mathrm{response},i}\left(N_{pix}\right) \quad = \quad -\frac{N_{\mathrm{eff},i}}{N_{\mathrm{pix}}} \cdot \log\left(1 - \frac{N_{\mathrm{pix}}}{N_{\mathrm{eff},i}}\right) \tag{3.4}$$

where $N_{\mathrm{eff},i}$ is the average effective number of pixels of a SiPM.

3.2.3. Temperature correction

The response of the SiPM changes with temperature. Therefore, the gain constant g_i and MIP constant M_i are both dependent on the temperature.

For the relevant temperature range between 20.2 and 25.8 °C, a linear approximation with the following parametrisation was made [15] to correct the calibration

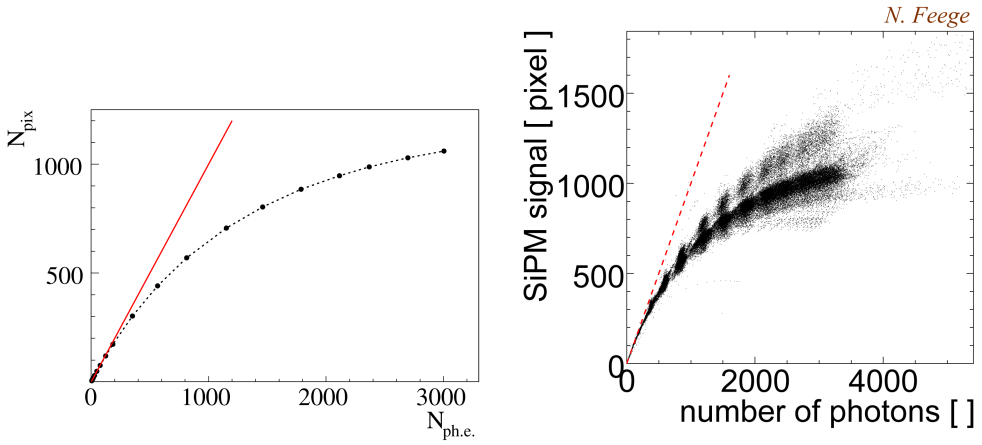

(a) (b)

Figure 3.5.: Non-linear response of a single SiPM (a) and for all SiPMs (b) where the number of pixels N_{pix} is a function of the number of photo-electrons $N_{\text{ph.e.}}$ [16].

constants for temperature effects:

$$g_i\left(T_i\right) = g_{\text{ref},i} + \frac{\mathrm{d}g_i}{\mathrm{d}T} \cdot \left(T_i - T^{\text{g}}_{\text{ref},i}\right) \tag{3.5}$$

$$M_i\left(T_i\right) = M_{\text{ref},i} + \frac{\mathrm{d}M_i}{\mathrm{d}T} \cdot \left(T_i - T^{\text{M}}_{\text{ref},i}\right) \tag{3.6}$$

where T_i is the temperature of the cell i. The values $g_{\text{ref},i}$ and $M_{\text{ref},i}$ are the calibration constants for the gain and MIP at the temperature $T^{\text{g}}_{\text{ref},i}$ and $T^{\text{M}}_{\text{ref},i}$, respectively.

The procedure to determine the temperature correction to the CERN 2010 data for the MIP constant (Eq. 3.6) is as follows. First a reference temperature $T^{\text{M}}_{\text{ref},i}$ of 25 °C has been chosen because it has the highest statistics in calibration data (Figure 3.6). For every cell i the MIP calibration constant $M_{\text{ref},i}$ is measured at that temperature (Figure 3.3.a).

The absolute slope $\mathrm{d}M_i/\mathrm{d}T$ can be determined per channel, but is in practice not feasible due to limited statistics for temperatures other than the reference temperature. Instead, the relative slope is determined per layer which is then used to calculate the absolute slope $\mathrm{d}M_i/\mathrm{d}T$ per channel. An example of the relative MIP calibration constant as function of the temperature in one layer is shown in Figure 3.7 where the red solid line is a linear fit.

3.3. Beam line setup

A sketch of the test beam is shown in Figure 3.8. It consists of the tungsten HCAL detector prototype itself (section 3.1), three wire chambers for measuring the beam position and profile, three scintillators for triggering and two Cherenkov threshold counters for particle identification. An additional wire chamber (T9 Wire Ch.) and scintillator (BXSCINT 1001) belong to the beam-line instrumentation and have not been connected to the CALICE DAQ.

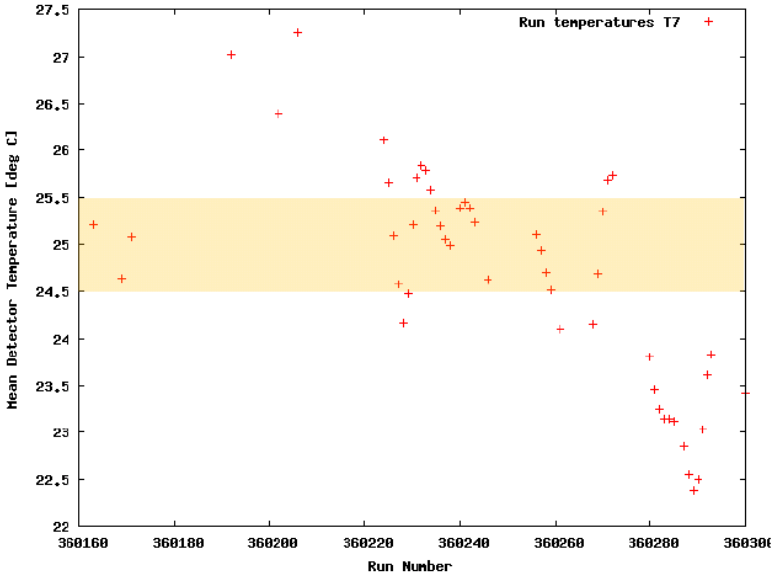

Figure 3.6.: The temperature vs. run number. The yellow band is the temperature range with the most statistics [17].

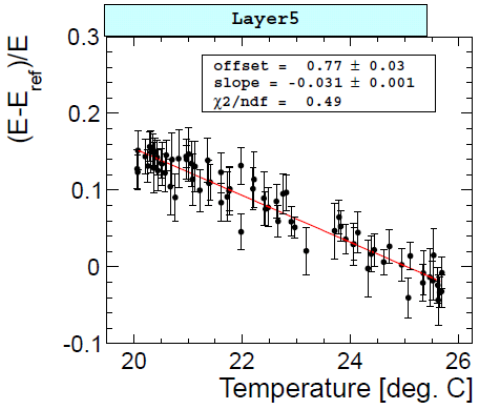

Figure 3.7.: An example for the temperature dependence of MIP constants for a single layer.

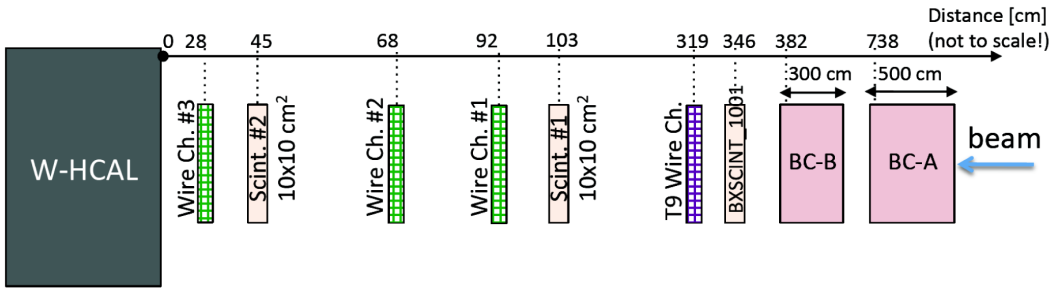

Figure 3.8.: Schematic representation of the test beam elements.

Table 3.2.: Cherenkov threshold values for CO_2 gas and various particles [18].

	Cherenkov threshold (bar absolute)				
Momentum (GeV)	Electron	Muon	Pion	Kaon	Proton
1	0.0003	13.61	23.91		
2	0.0001	3.38	5.92		
3	0.0000	1.50	2.63	33.40	
4	0.0000	0.84	1.48	18.64	
5	0.0000	0.54	0.94	11.88	43.68
6	0.0000	0.38	0.66	8.24	30.11
7	0.0000	0.28	0.48	6.04	22.02
8	0.0000	0.21	0.37	4.62	16.81
9	0.0000	0.17	0.29	3.65	13.26
10	0.0000	0.14	0.24	2.96	10.73

3.4. Particle identification

A setup of two Cherenkov threshold counters (A and B) filled with CO_2 is used for the first level of particle identification in the offline analysis. This section will start with a description of how a counter can identify a particle. It is followed by a discussion on the electron tagging efficiency, which leads to the turn-on curve. Taking the efficiency into account, the general strategy is explained for separating electrons, muons and pions, and protons. Inefficiency leads to contamination, the impurity of the samples is therefore examined. This section concludes with the determination of the beam composition.

A charged particle going through the counter emits Cherenkov radiation when its velocity is higher than the speed of light in the gas. This depends on the refraction index of the gas and can be varied by changing the pressure. Whether the Cherenkov counter gives a signal (tag) or not thus depends on the gas pressure in the counter and on the particle's velocity. Table 3.2 shows the threshold pressure values for various particles depending on its momentum. When the gas pressure exceeds the threshold value, a charged particle with a given momentum will emit Cherenkov light. The maximum safe operating pressure for the counters is 3.5 bar absolute.

3.4.1. Electron tagging efficiency

The electron tagging efficiencies for the two Cherenkov counters have been measured at 1 GeV and is shown in Figure 3.9 for different pressures. The number of photons created within the acceptance of the photomultiplier increases approximately linearly with increasing pressure above threshold (~0 bar for electrons), leading to a turn-on curve. Each point is measured by setting both Cherenkov counters to the same pressure and using a tag-and-probe method. The efficiency for a given pressure can

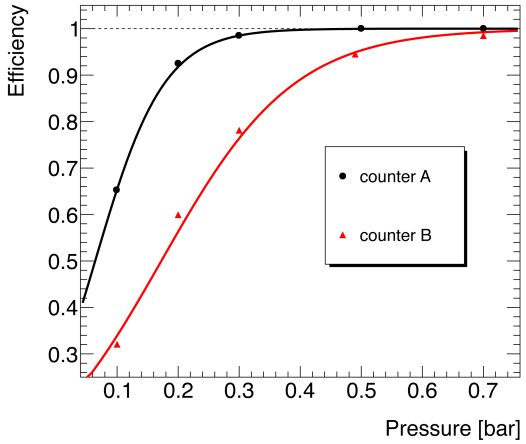

Figure 3.9.: Efficiencies of the two Cherenkov counters in the beam line [19].

then be calculated with

$$\epsilon_{\mathrm{A}}(P) = 1 - \frac{N_{\overline{\mathrm{A}}\&\mathrm{B}}}{N_{\mathrm{B}}} \tag{3.7}$$

$$\epsilon_{\mathrm{B}}(P) = 1 - \frac{N_{\mathrm{A}\&\overline{\mathrm{B}}}}{N_{\mathrm{A}}} \tag{3.8}$$

where N is the number of events for logical combinations of the signals of A and/or B e.g. $N_{\mathrm{A}\&\overline{\mathrm{B}}}$ is the number of events where counter A has a signal and counter B has no signal.

The higher efficiency of A compared to B is due to the longer length of the counter. This is 5 m for A and 2.5 m for B.

3.4.2. Selection strategy

The general strategy, taking the efficiencies and pressure limits into account, is to use counter A for separating electrons from muons and pions, and to use counter B to separate muons and pions from protons. The exact pressures used can be found in Appendix A. The following logical combinations of the signals of A and B are used to select the particles (protons for positive runs only):

$$\text{Electrons} = \mathrm{A}\&\mathrm{B} \tag{3.9}$$

$$\text{Muons and pions} = \overline{\mathrm{A}}\&\mathrm{B} \tag{3.10}$$

$$\text{Protons} = \overline{\mathrm{A}}\&\overline{\mathrm{B}} \tag{3.11}$$

At 1 and 2 GeV, the electron threshold is the only one within the pressure limits. Consequently, only electrons can be separated at those momenta. The particle identification using the Cherenkov threshold counters becomes critical for the energies 1 and 2 GeV. The shower shapes for the electrons and pions are similar in this energy regime. They are hard to separate in the data analysis, therefore the tagging is the only means of selecting the electrons.

For higher momenta ($p_{\mathrm{beam}} \geq 7\,\mathrm{GeV}$) the electron content is low (Table 3.4). Priority was given to tag electrons efficiently, the pressure was therefore set above

the muon threshold in most runs considered for this analysis. While the electron sample is now contaminated with muons, the muons can be rejected in the off-line analysis (section 5.1).

The pion selection include muons due to in-flight decays. Similar to the contaminated electrons at higher momenta ($p_{\text{beam}} \geq 7\,\text{GeV}$), the muons are rejected in the off-line analysis (section 6.1).

3.4.3. Impurity due to tagging inefficiency

A particle selection is pure when only the intended particle type is in the selection. When other particle types are also selected, the selection becomes contaminated. When a counter is used in veto mode, the inefficiency becomes a source of contamination.

Cherenkov A is always set to tag electrons. It is 100% efficient at low momenta ($P > 0.4\,\text{bar}$) and gets less efficient for higher momenta ($p_{\text{beam}} \geq 7\,\text{GeV}$), but the electron fraction becomes in the order of one percent. Electron contamination in pion and proton selection should therefore be well below one percent in all cases.

Cherenkov B is set to tag muons and pions with a pressure of 3 bar absolute. As discussed before, at 1 and 2 GeV it is not possible to separate pions from protons with Cherenkov counters.

Contamination due to tagging inefficiency is expected for the proton selection (Eq. 3.11) at 3 GeV. Counter A has a pressure of 1 bar absolute and is thus 100% efficient for e^+ tagging. No contamination from positrons is therefore expected. The pion threshold is 2.63 bar absolute while counter B has a pressure of 3 bar absolute. Assuming the turn-on curve is the same for pion as for electrons (Figure 3.9) the counter tags only 88% (at 3 - 2.63 = 0.37 bar absolute) of the pions. The remaining 12% has now become a source of contamination for the proton selection. The proton selection has a contamination of 28% ($= 69\% \cdot 12\% / (69\% \cdot 12\% + 21\%)$) with pions. For $p_{\text{beam}} \geq 4\,\text{GeV}$ counter B is 100% efficient, no contamination is consequently expected for the proton selection.

3.4.4. Impurity due to muons

It is observed in the analysis (section 5.1) that there are muons and pion-like events in the electron selection, even when the pressure is set below the thresholds for muons and pions. The fraction of muons in the e^+/e^- selection is shown in Table 3.3 for different beam momenta and counter pressures. The number of muons is determined by counting the events in the muon peak as described in section 5.1.

The occurrence of muon events in the e^+/e^- selection can be explained as follows. For a given beam momentum, the pressure of counter A is set below the threshold pressure of muons and therefore no muons are expected. However, the threshold depends on the momentum of the particle. Muons with higher momenta can therefore get tagged. Such muons can be created upstream close to the target but outside the acceptance of the momentum selection magnet and with a direction towards the Cherenkov counters and the detector.

Table 3.3.: Fraction of muons in e^+/e^- selection for data where A is set below the muon threshold for the given momentum.

		Muons in particle selection (%)	
p_{beam} (GeV)	Cher-A (bar abs.)	e^-	e^+
1	0.1-0.7	< 1	< 1
2	1.0	< 1	< 1
3	1.0	1	6
4	0.6	2	2
5	0.3	3	N/A
5	0.4	18	11
6	0.2	8	N/A
6	0.3	30	N/A
6	0.35	69	50
7	0.15	N/A	8
7	0.23	N/A	43

Table 3.4.: Beam composition for positive polarity.

	Fraction in beam (%)		
p_{beam} (GeV)	e^+	$\mu^+ + \pi^+ + p$	
1	76	24	
2	28	72	
	e^+	$\mu^+ + \pi^+$	p
3	10	69	21
4	3	67	30
5	1	63	36
6	< 1	60	39
7	< 1	55	43
8	< 1	48	51
9	< 1	39	60
10	< 1	31	68

3.4.5. Beam composition

The beam contains multiple particle types. The content is shown in Table 3.4 for the positive polarity and in Table 3.5 for the negative polarity. The beam composition is estimated using the Cherenkov counters. The fractions are corrected for the efficiency using the electron tagging efficiency. It is assumed that the hadron turn-on curve is similar to the electron turn-on curve. In the case that counter A is set to tag electrons only, the counter is not corrected for impurity due to muons as either the fraction of muons or the fraction of electrons is small.

As discussed earlier in this section, the selection strategy is different depending on the beam momentum. The beam composition for positive polarity is calculated

Table 3.5.: Beam composition for negative polarity.

	Fraction in beam (%)	
p_{beam} (GeV)	e^-	$\mu^- + \pi^-$
-1	85	15
-2	40	60
-3	16	84
-4	6	94
-5	4	96
-6	2	98
-7	2	98
-8	1	99
-9	1	99
-10	1	99

as follows where $N_{\{A,B\}}$ denotes the number of events tagged by counter A or B, $N_{\overline{B}}$ the number of events not tagged by B, N the total number of events, and $\epsilon_{\{A,B\}}$ the electron tagging efficiency:

- 1 - 2 GeV

$$\text{Fraction}\left(e^+\right) = \frac{N_A}{\epsilon_A}/N \tag{3.12}$$

$$\text{Fraction}\left(\mu^+ + \pi^+ + p\right) = 1 - \frac{N_A}{\epsilon_A}/N \tag{3.13}$$

- 3 - 10 GeV

$$\text{Fraction}\left(e^+\right) = \frac{N_A}{\epsilon_A}/N \tag{3.14}$$

$$\text{Fraction}\left(\mu^+ + \pi^+\right) = \left(\frac{N_B}{\epsilon_B} - \frac{N_A}{\epsilon_A}\right)/N \tag{3.15}$$

$$\text{Fraction}\left(p\right) = 1 - \frac{N_B}{\epsilon_B}/N \tag{3.16}$$

For the negative polarity, it is

- 1 - 10 GeV

$$\text{Fraction}\left(e^+\right) = \frac{N_A}{\epsilon_A}/N \tag{3.17}$$

$$\text{Fraction}\left(\mu^+ + \pi^+\right) = 1 - \frac{N_A}{\epsilon_A}/N \tag{3.18}$$

4
Analysis chain overview

This chapter provides an overview of the analysis chain which is illustrated in Figure 4.1. A block represents a process while arrows represent a flow of information between processes. Three flows can be distinguished:

1. test beam data* (solid green line),
2. Monte Carlo simulated data (dashed red line),
3. calibration data (dot-dashed blue line).

It will now be explained how the flows and processes interact with each other, starting with the reconstruction step. Event selection and analysis will be discussed separately for electrons (chapter 5), and for pions and protons together (chapter 6).

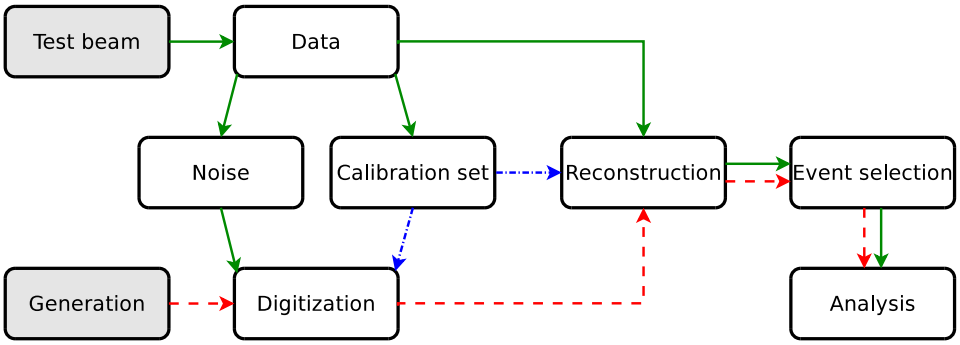

Figure 4.1.: Overview of the analysis chain. The green solid lines represents test beam data. The red dashed lines are Monte Carlo simulated data. The blue dot-dashed lines are calibration data that is used for both reconstruction and digitization.

*The usage of the term *data* can be confusing in an environment where physics and computing is present. Whereas in physics *data* means the measurements from an experiment, *data* in computing is in itself a ambiguous term and can refer to any kind of information.

The principal unit used in the analysis is MIPs while the data from the detector are in units of ADC counts. Reconstruction is the calibration of the uncalibrated data. The measurement of the calibration constants from uncalibrated data is discussed in section 3.2.

The Monte Carlo is generated with GEANT4 [12], a simulation software for particles interacting with matter. Different physics models exists for describing hadronic interactions for different energy regimes. The models [20] relevant to the analysis are:

- The Quark-Gluon String Precompound (QGSP, $E > 12\,\text{GeV}$) model is built from several component models which handle various parts of a high energy collision. The quark-gluon string (QGS) part handles the formation of strings in the initial collision of a hadron with a nucleon in the nucleus. String fragmentation into hadrons is handled by the Quark-Gluon String fragmentation model. The precompound part handles the de-excitation of the remnant nucleus.

- The FRITIOF Precompound (FTFP, $E > 4\,\text{GeV}$) model is built from several component models which handle various parts of a high energy collision. The FRITIOF part handles the formation of strings in the initial collision of a hadron with a nucleon in the nucleus. String fragmentation into hadrons is handled by the Lund fragmentation model. The precompound part handles the de-excitation of the remnant nucleus.

- Low Energy Parametrised (LEP) is mainly used to either fill the gaps between the validity interval of the other models, or for particle species the other models cannot describe.

- Bertini intra-nuclear cascade model (BERT, $E \leq 9.9\,\text{GeV}$) considers the nucleus as a Fermi gas of nucleons where the interaction with the incoming projectile is treated as a series of independent and incoherent collisions.

- Binary Cascade (BIC) generates the final state for hadron inelastic scattering by simulating the intra-nuclear cascade. The target nucleus is modeled by a 3-D collection of nucleons, as opposed to a smooth nuclear medium. The propagation through the nucleus of the incident hadron and the secondaries it produces is modeled by a cascading series of two-particle collisions. These collisions occur according to the particles' total interaction cross section. Secondaries are created during the decay of resonances formed during the collisions. Due to its dependence on resonances, it should not be used for pions above 1.3 GeV.

- Neutron High Precision model (HP, $E < 20\,\text{MeV}$) is data driven and transports neutrons below 20 MeV to thermal energies.

To cover the full energy range, the models are combined into what is called a physics list. GEANT4 includes several physics lists and the following are used in the analysis: QGSP_BERT, QGSP_BERT_HP, QGSP_BIC_HP, and FTFP_BERT_HP. Figure 4.2 shows the various physics lists with the energy ranges of the models. In

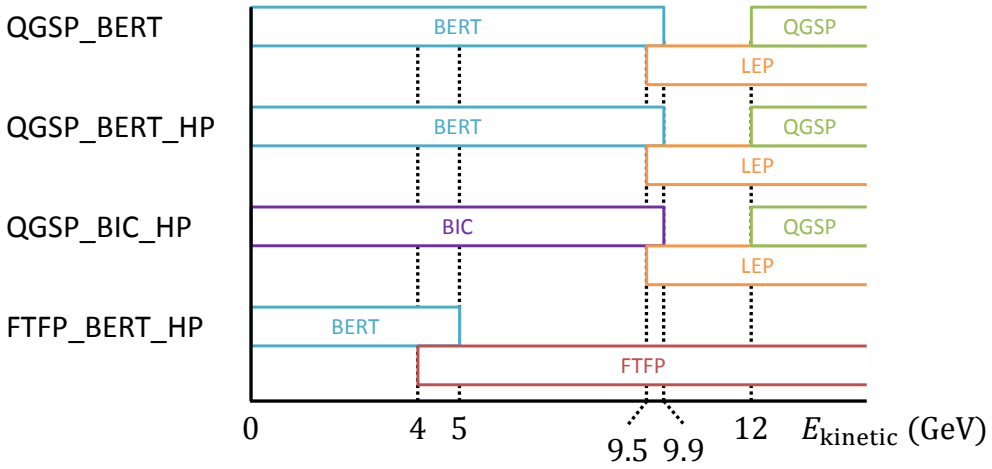

Figure 4.2.: Physics lists in GEANT4 that are used in this analysis: QGSP_BERT, QGSP_BERT_HP, QGSP_BIC_HP, and FTFP_BERT_HP. Each physics list is composed of different physics models describing different energy ranges.

the transition region of two models, a model is chosen randomly with a probability that is linear with the energy.

The inclusion of Neutron High Precision model (HP) in a list makes a difference for hadronic physics with high Z materials (such as tungsten) and is illustrated with 10 GeV π^+. The energy sum distribution for the data is shown in Figure 4.3, together with QGSP_BERT and QGSP_BERT_HP. The difference in the mean between data and QGSP_BERT is 5% whereas it is 0.5% between data and QGSP_BERT_HP. The HP model is therefore used for the pions and protons Monte Carlo.

At the generation step, a particle is generated of given type, energy, origin and direction. The direction is always set parallel to the z-axis. The particle interacts with the detector material, and the energy depositions resulted from those interactions are recorded in an event. To simulate an actual detector response, the depositions in the active material are digitized [21].

To match the beam profile of the data, the origin of the Monte Carlo particle is varied. The parameters varied in the Monte Carlo are the position of the origin in x, y and z and the Gaussian smearing parameters in the position: σ_x, σ_y, and σ_z.

The matching of the beam profile between data and Monte Carlo is an iterative process. The initial x- and y-position are the mean of the profile in x and y, respectively. The spread of the beam is affected by the smearing in the position σ_x, σ_y, but also by the z-position of the origin and the beam momentum.

An example of the beam profile for 3 GeV electrons is shown in Figure 4.4. The agreement between data and Monte Carlo is good.

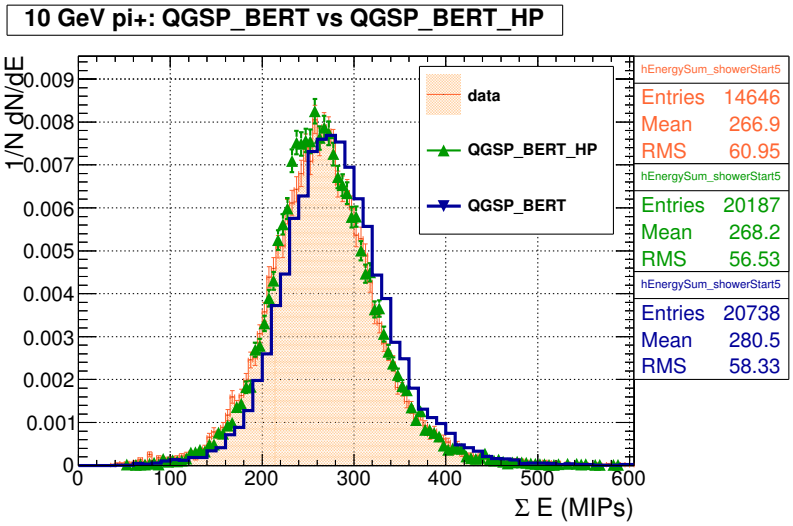

Figure 4.3.: The energy sum distribution of data (orange filled histogram) is shown here for 10 GeV π^+. Two physics lists, QGSP_BERT_HP (green triangles) and QGSP_BERT (blue solid line), are compared to data.

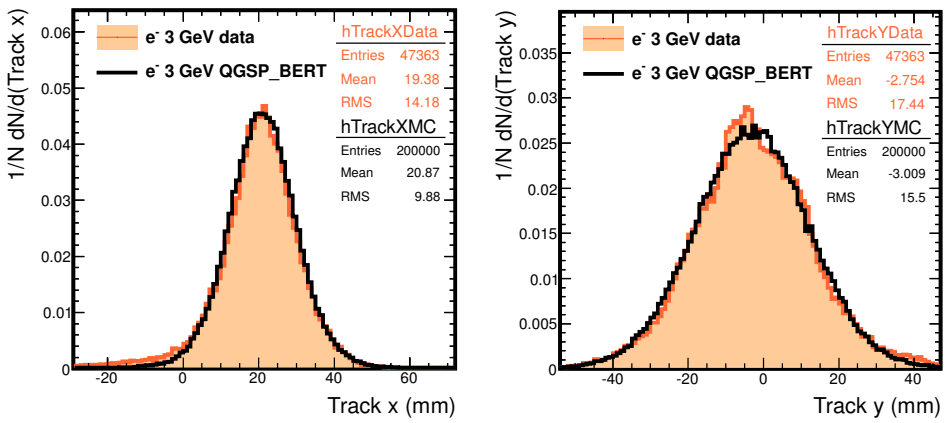

(a) (b)

Figure 4.4.: Beam profile for 3 GeV electrons in x (a) and y (b).

5 Electrons

The development of electromagnetic showers from an incident electron or photon is a well understood process. The comparison between data and Monte Carlo is thus used to check the analysis chain. The event selection is discussed in section 5.1 while the rest of the section is dedicated to the analysis which consists in the measurement of the linearity, energy resolution, longitudinal profile and mean shower radius.

Only the physics list QGSP_BERT is compared to the data. The various physics lists have the same models for electromagnetic interactions and differ only in the hadronic models. As a consequence, the differences in Monte Carlo between e^- and e^+ are due to systematic effects.

5.1. Event selection

Only data in the energy range 1 to 6 GeV are considered. Data at higher energies ($E \geq 7\,\mathrm{GeV}$) are rejected because of the very low electron content of the beam at these energies.

The Cherenkov threshold counters are used as a first selection of electrons in data. However, muons created upstream at higher energies can contaminate the sample (section 3.4).

An additional rejection is based on the shower center and the number of hits. The shower center k_{COG} is quantified by the center of gravity of the hits i, weighted by its energies E_i

$$k_{\mathrm{COG}} = \frac{\Sigma E_i \cdot k_i}{\Sigma E_i} \tag{5.1}$$

where k is the detector depth expressed in layers. The first layer of the detector starts at $k = 1$. An example of a distribution of the events for 6 GeV data after selecting electrons using the Cherenkov counters, depending on k_{COG} and the number of hits, is shown in Figure 5.1. The muons have a k_{COG} that is in the center of the detector. The pions don't have a peak and are scattered everywhere instead. Electrons are

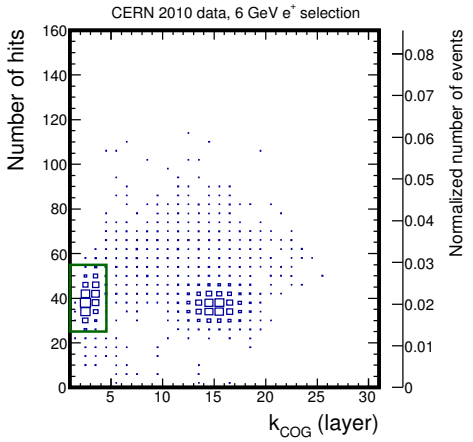

Figure 5.1.: The number of hits against k_{COG} (Eq. 5.1) for 6 GeV data events, selected on electrons using Cherenkov counters. Events inside the solid green box are selected.

identified as events with a k_{COG} in the first few layers. Those events which fulfill the cuts defined by the solid green box are selected.

The shower center can help in the particle identification. The electron showers are contained due to the radiation length of 0.35 cm in tungsten [8]. The pion interaction length, on the other hand, is 11.33 cm. The pion can therefore go deeper into the detector before it starts to shower. The shower itself will also be longer and broader than an electron shower. Muons are minimal ionizing particles and go through the whole detector depositing a similar amount of energy in each layer. The k_{COG} for muons is thus in the center of the detector.

In a third selection step, noise hits are rejected based on distance from the shower axis and the z-position of the hits. Electrons in the energy range relevant for this analysis are contained in a small region. This region is described by a cylinder with a radius of 50 mm (5.3 R_M) with respect to the shower axis and a depth of 20 layers [22]. Hits outside this region are likely to be noise and are discarded.

5.2. Energy sum distribution

The energy sum ΣE_i of a single event is the sum of the energy of the hits i within 50 mm of the shower axis. The hit energy E_i is pedestal subtracted and above the noise cut.

For low energies ($E \leq 5$ GeV) the energy sum distribution shows non-Gaussian tails towards large energy sums. An example for 1 GeV electrons is shown in Figure 5.2.a. With increasing energy the distribution becomes Gaussian (Figure 5.2.b). The line shape can be described by the Novosibirsk function:

$$f(x) \quad = \quad A \cdot \exp\left(-0.5 \cdot \frac{\ln^2\left[1 + \Lambda \cdot \tau(x-\mu)\right]}{\tau^2} + \tau^2\right) \tag{5.2}$$

where

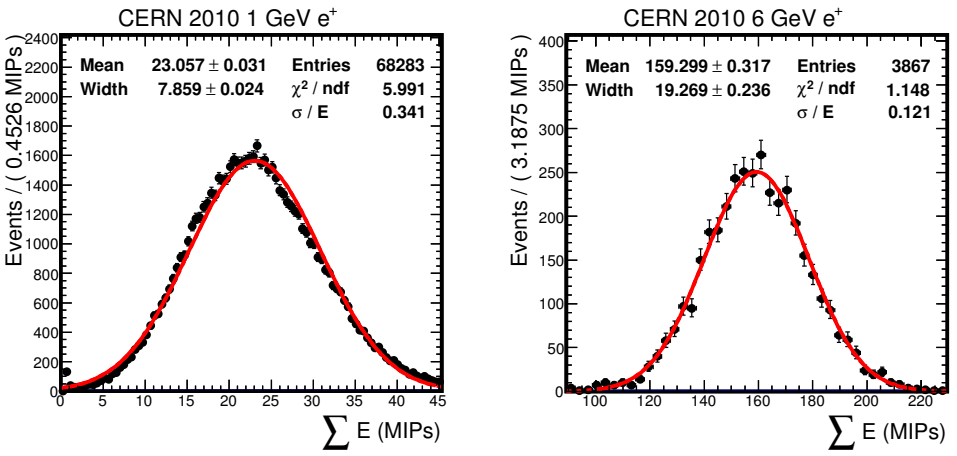

(a) (b)

Figure 5.2.: Energy sum distributions are shown for 1 GeV (a) and 6 GeV (b) positrons. The red curve is a Gaussian fit. Whereas the distribution for 6 GeV is well described by the Gaussian fit, for 1 GeV it shows a tail towards large energy sums.

$$\Lambda = \frac{\sinh\left[\tau \cdot \sqrt{\ln 4}\right]}{\sigma \cdot \tau \cdot \sqrt{\ln 4}} \tag{5.3}$$

Similar to a Gaussian, it has a mean μ and a width σ. In addition, it has a third parameter τ which accounts for the tail. A τ of zero means that the shape is Gaussian.

We assume the origin of the asymmetry is statistical. The central limit theory states that the distribution of a sum (or equally, an average) becomes Gaussian-like with increasing number of independent variables (summants) per sum. This is demonstrated in Figure 5.3 as a simplified mathematical exercise. Ten million numbers are drawn from the single hit energy distribution (a) in a toy Monte Carlo experiment. This distribution does not represent actual calorimeter data and is for illustrative purposes only. The numbers are then divided into groups of fixed size and the average of each group is calculated. A group is analogous to an event with the group size given by the number of hits from data. The distribution of the average for a group size of 8 numbers is shown in (b) where the tail towards large energies is clearly visible. On average, 1 GeV electrons have 17 hits per event (c) whereas 6 GeV electrons have 38 hits per event (d). With increasing number of hits per event, the energy sum distribution becomes more Gaussian as stated by the central limit theory.

5.3. Linearity

The calorimeter signals are generated by the active media due to ionization and/or excitations. An incident electron showers into an electromagnetic cascade consisting

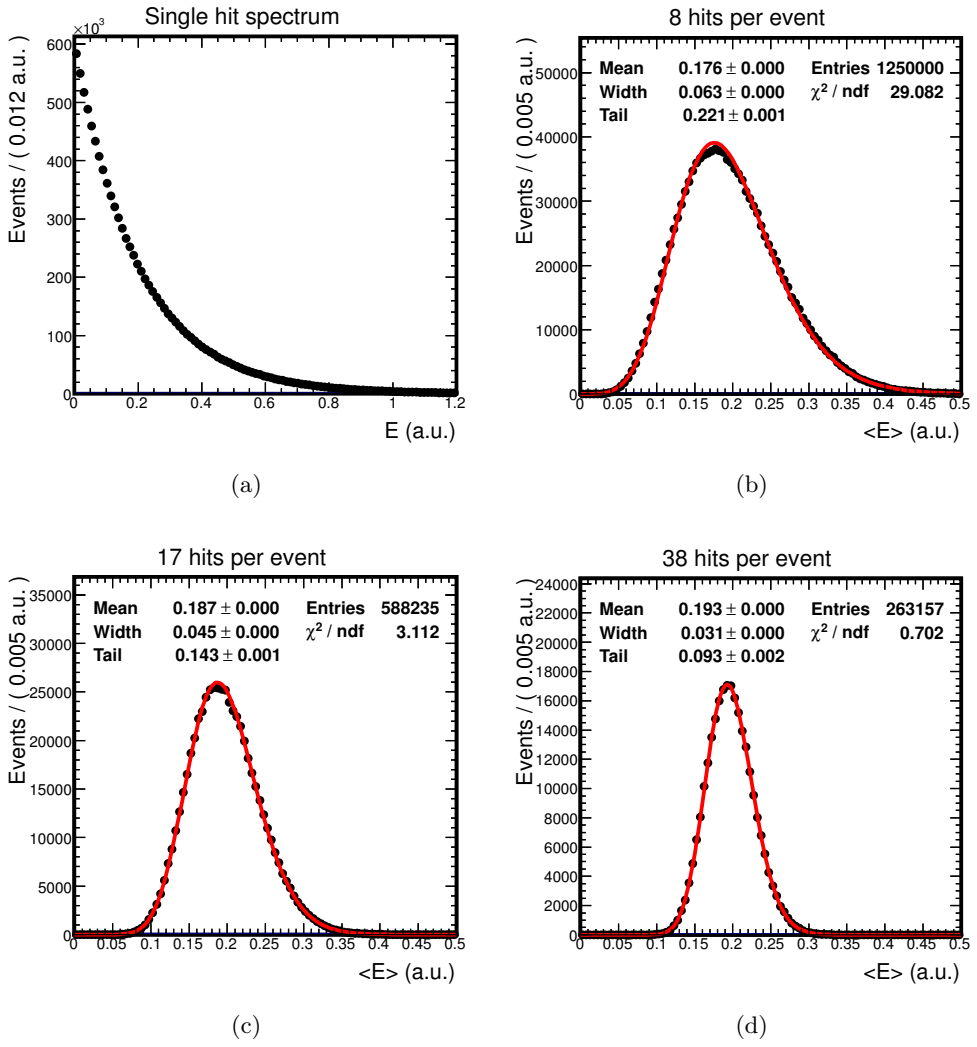

Figure 5.3.: Three distributions of averages with 8 hits per event (b), 17 hits per event (c), and 38 hits per event (d). The value of each hit is drawn from a Monte Carlo single hit spectrum (a). The red curve is a fit with the Novosibirsk function (Eq. 5.2).

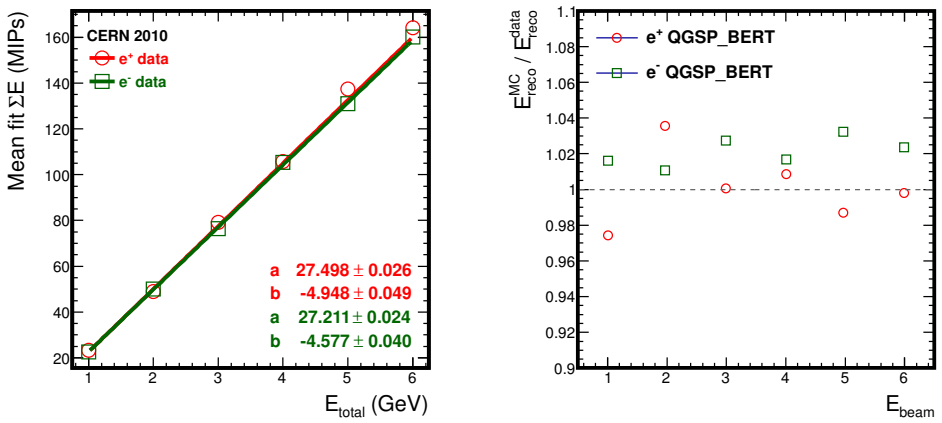

(a) (b)

Figure 5.4.: The detector response for electrons (green) and positrons (red) for data (left plot). The solid line is a fit of the function $E_{\text{reco}} = a \cdot E_{\text{total}} + b$. The data are compared to Monte Carlo (QGSP_BERT physics list) in the right plot (b).

Table 5.1.: Electromagnetic scale of the W-AHCAL detector for electrons and positrons. The detector response (Figure 5.4) is fitted with $E_{\text{reco}} = a \cdot E_{\text{available}} + b$ and the fitted values for the parameters are listed here.

parameter	e^+	e^-
a (MIPs/GeV)	27.50 ± 0.03	27.21 ± 0.02
b (MIPs)	-4.95 ± 0.05	-4.58 ± 0.04

purely of photons and electrons. The detector response should therefore be linear to electrons (and photons) with respect to their energy.

Deviation from signal linearity might indicate problems with the calibration. It can also be caused by instrumental effects such as saturation and shower leakage. This is however not expected for electrons with energies between 1 and 6 GeV.

The reconstructed energy E_{reco}, in units of MIPs, is determined as the mean value of the fit of the energy sum distribution as described in section 5.2. The dependence of E_{reco} on the beam energy is shown in Figure 5.4.a for electrons (green squares) and positrons (red circles). The lines correspond to a fit with the function

$$E_{\text{reco}} \quad = \quad a \cdot E_{\text{available}} + b \tag{5.4}$$

where the fitted values for the parameters are summarized in Table 5.1.

The reconstructed energy of the Monte Carlo is within 4% of the data and is shown in Figure 5.4.b.

Systematic errors

The statistical uncertainty of the fitted value is up to 0.33% at 6 GeV. The sources of systematic uncertainties include temperature correction, determination of the SiPM

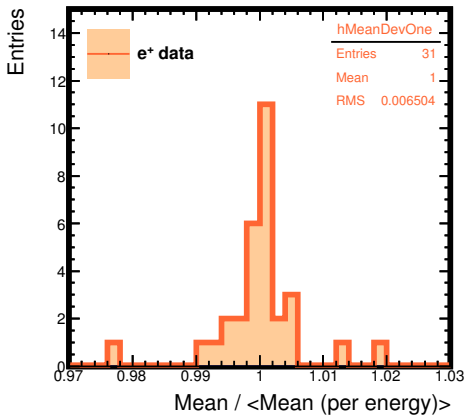

Figure 5.5.: The reconstructed energies per run relative to the average of E_{reco} per energy point for e^+ data.

gain, and the determination of the SiPM saturation level. Only the statistical uncertainty and the temperature correction systematic error is included in the linearity plot. The impact of the systematic uncertainty of the SiPM response on the reconstructed energy has not been studied. It is explained in the last paragraph what is required to do for a follow up study.

The systematic error of the temperature correction is determined from the distribution of the relative reconstructed energy (Figure 5.5) as the one standard deviation spread. This distribution is constructed in two steps. First, for each run the mean of the energy sum is calculated. Second, the mean of the energy sum is compared to the average of the reconstructed energies of the corresponding beam energy. The one standard deviation spread of the resulting distribution is 0.7%.

The systematic uncertainty on the SiPM gain determination is 2% and is due to the stability of the fit [22].

The response curve of the SiPMs has been measured by illuminating all pixels. In the detector, however, the SiPMs are attached to a wavelength-shifting (WLS) fiber. The fiber has a radius of 1 mm while the active area of the SiPM is 1 mm^2. The geometric ratio of 79% is in agreement with the measured value of 80.5%. The measured response curve for all the SiPMs are therefore rescaled with the average factor of 80.5%. Not all channels are identical; applying a single rescaling factor to all channels introduces a systematic error on the saturation level of 11.3% [22].

The determination of both the gain and the saturation level has systematic errors. The impact of it on the reconstructed energy has however not been studied. A follow up study would require to do toy Monte Carlo experiments. Each experiment will have a different rescaling factor. Each factor is taken from a Gaussian distribution with a mean of 0.80 and a sigma of 0.09. The one standard deviation spread of the reconstructed energies from all the toy Monte Carlo experiments is then taken as the systematic uncertainty.

Table 5.2.: The energy resolution of the W-AHCAL and the Fe-AHCAL [23] for e^+/e^-. The noise term c is determined in two ways: from the fit and from noise events.

	W-AHCAL		Fe-AHCAL	
	e^+	e^-	e^+	e^-
Stochastic term a (% $GeV^{1/2}$)	28.7 ± 0.1	27.9 ± 0.1	21.9 ± 1.4	21.7 ± 0.2
Constant term b (% GeV)	0.0 ± 3.6	0.0 ± 3.6	1.0 ± 1.0	0.0 ± 0.8
Noise term c (MeV), fit	190 ± 4	202 ± 3		
Noise term c (MeV), noise events	53	56	58	50

5.4. Energy resolution

The energy resolution (see section 2.2) indicates the precision of the measurement of an incident particle's energy. It is expected to be the same for electrons and positrons. When comparing tungsten to iron, it is expected that iron gives a better resolution for e^+/e^- due to the higher sampling fraction.

The resolution is estimated as the ratio between the width and the mean of the fit of the energy sum distribution. The fit function is the Novosibirsk function as described in section 5.2 and the fit range is $\pm 3\sigma$ from the mean. The initial mean and width are determined by a Gaussian fit of up to 10000 events.

The energy resolution for the electron and positron data is shown in Figure 5.6.a as a function of the beam energy. The solid lines are fits of the data points are the function (Eq. 2.3). The fitted values are shown in Table 5.2.

The noise term c can also be measured from noise events. Noise events are randomly triggered events during data taking to measure the pedestal offset and noise. The noise term c is the RMS of the reconstructed energy distribution of the noise events. Figure 5.7 shows the contribution of the noise to the energy resolution per beam energy. The average noise for both electrons and positrons is 2 MIPs. This value is converted to GeV by scaling it with the electromagnetic conversion factor a as determined in section 5.3. Using this method, the noise term c is between 53 and 56 MeV, which is roughly a factor 4 smaller than the values obtained from the fit but agrees with the iron calorimeter result. This is not yet understood and requires additional study.

Compared to the Fe-AHCAL, the detector with the tungsten absorbers has worse resolution for e^+/e^- (Figure 5.6.b, Table 5.2). This is expected due to the shorter radiation length of tungsten.

The energy resolution for the Monte Carlo agrees within 5.5% with the data as shown in Figure 5.6.c.

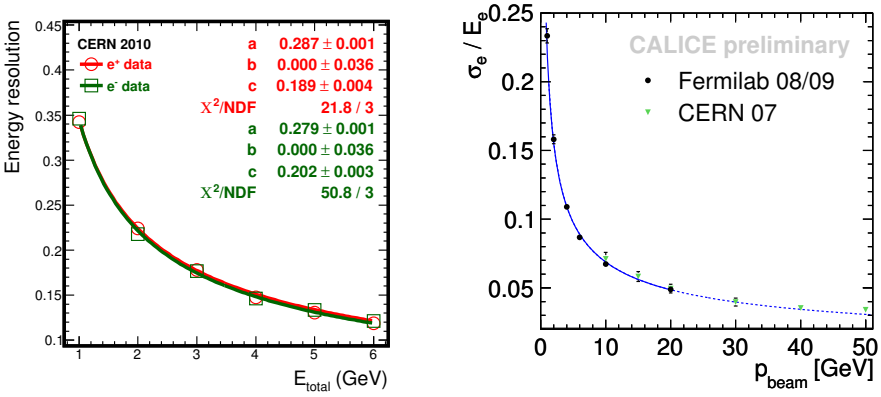

(a) W-AHCAL (b) Fe-AHCAL

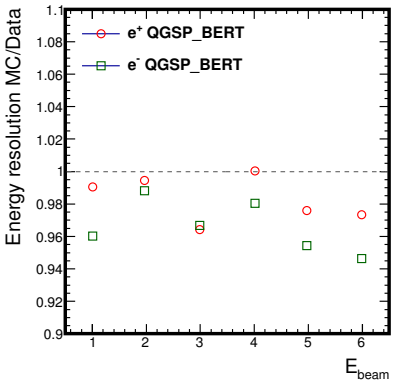

(c)

Figure 5.6.: Energy resolution for electrons (green) and positrons (red) for the tungsten AHCAL (a). The solid line is the fit of the resolution with Eq. 2.3. The resolution for the iron AHCAL [23] is shown in (b). Tungsten AHCAL data are compared to QGSP_BERT in (c).

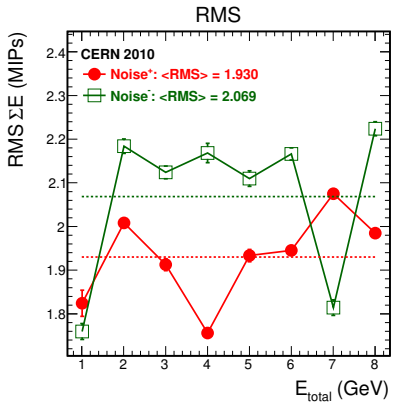

Figure 5.7.: The RMS of the reconstructed energy, in units of MIPs, for noise events is a measure for the noise term c in the energy resolution, in units of GeV. The dashed lines indicate the average RMS.

Table 5.3.: The critical energy ϵ_c for iron and tungsten [8].

Material	ϵ_c for e^- (MeV)	ϵ_c for e^+ (MeV)
Iron (Fe)	21.68	21.00
Tungsten (W)	7.97	7.68

Table 5.4.: Fitted values for the critical energy ϵ_c.

	ϵ_c for e^- (MeV)	ϵ_c for e^+ (MeV)
Data	14.29 ± 0.02	14.04 ± 0.02

5.5. Longitudinal profile

The shower development along the beam axis can be described by the longitudinal profile [24], i.e. the energy density

$$\frac{\mathrm{d}E}{\mathrm{d}t} = a \cdot t^w \cdot e^{-bt} \tag{5.5}$$

where t is the shower depth, a a normalization constant, and both w and b are energy and material dependent parameters. When the shower depth t is expressed in units of radiation lengths, the position of maximum energy deposition t_{max} is

$$t_{max} = \ln\left(\frac{E}{\epsilon_c}\right) - 0.5 \tag{5.6}$$

where E is the energy of the particle inducing the shower. The critical energy ϵ_c is the energy at which an electron loses as much energy in collisions as in radiation. This is a material property. Values for iron and tungsten are shown in Table 5.3.

The longitudinal profiles for electrons for the energies 1 and 6 GeV are shown in Figure 5.8. Each bin has a width of 3.1 X_0 (1 layer) and is centered on the position of the active material. The data are fitted with Eq. 5.5 in the range 1.44 X_0 and 31 X_0 (10 layers).

The shower maximum is shown in Figure 5.9.a as a function of the beam energy. The points are fitted with Eq. 5.6 where the critical energy ϵ_c is a free parameter. The data point at 1 GeV is excluded from the fit because the shower maximum occurs in the first layer. The fitted values are shown in Table 5.4. The fitted values are between the critical energy of iron and tungsten (Table 5.3).

Figure 5.9.b shows the comparison of the Monte Carlo with the data for the shower maximum. The difference is at most 2%.

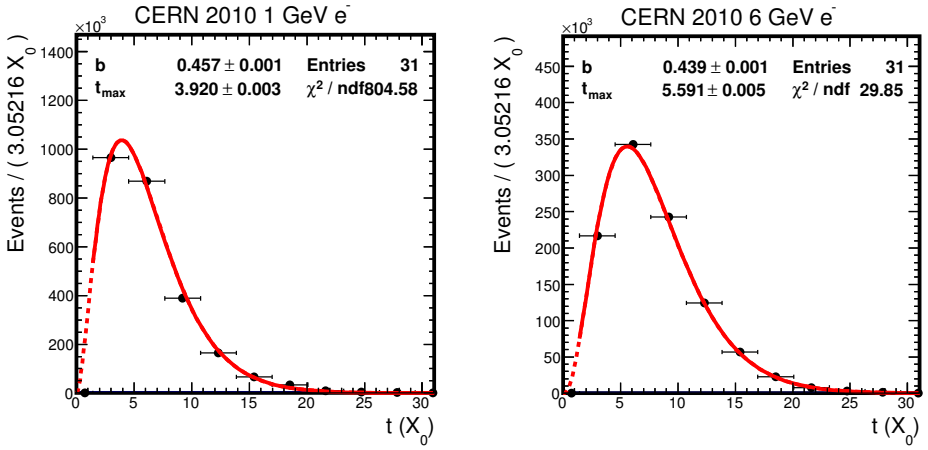

(a) (b)

Figure 5.8.: Longitudinal profile for 1 GeV e^- (a) and 6 GeV e^- (b). The red line is the fit of the data with Eq. 5.5 in the range where the line is solid. The dashed red line is the fitted function outside the fit range.

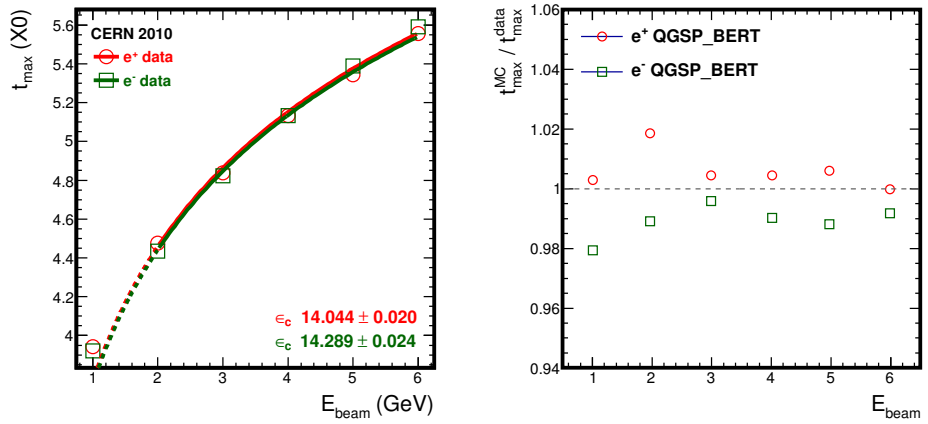

(a) (b)

Figure 5.9.: (a) Position of the shower maximum $t_{\max}$ as a function of the beam energy for positrons (red circles) and electrons (green squares). The solid lines are fit of Eq. 5.6 in the range 2 GeV and 6 GeV. The dashed line is the extension of the fit to 1 GeV. (b) The Monte Carlo compared to data.

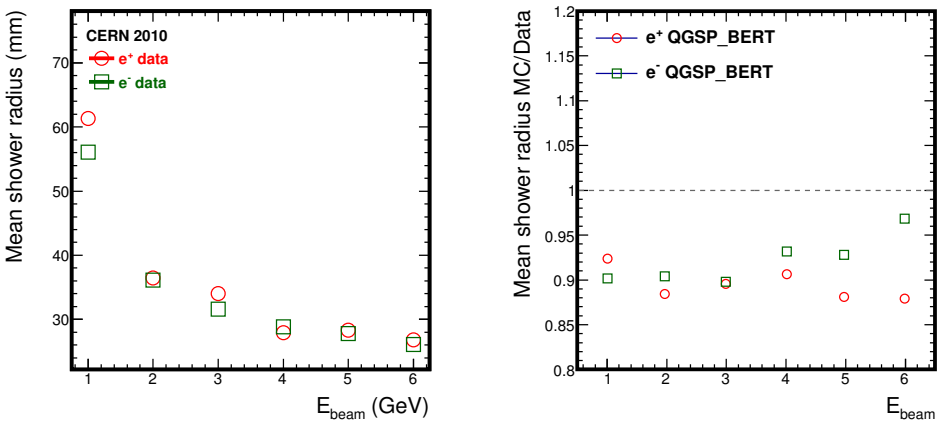

(a) (b)

Figure 5.10.: The mean shower radius (Eq. 5.7) versus the beam energy (a) for positrons (red circles) and electrons (green squares). On the right (b), the Monte Carlo is compared to the data.

5.6. Mean shower radius

In the plane transverse to the beam axis, the shower can be described by the mean shower radius

$$\langle R \rangle = \frac{\Sigma E_i d_i}{\Sigma E_i} \tag{5.7}$$

where i is a hit, E_i is the energy of that hit and

$$d_i = \left[(x_i - x_{\text{track}})^2 + (y_i - y_{\text{track}})^2 \right]^{\frac{1}{2}} \tag{5.8}$$

is the distance between the hit and the track. The position of the hit is the center of the calorimeter cell and is given by (x_i, y_i). The position of the track $(x_{\text{track}}, y_{\text{track}})$ is determined from the wire chambers.

The energy dependency of the mean shower radius is shown in Figure 5.10.a. As the beam energy increases from 1 to 6 GeV, $\langle R \rangle$ decreases from 62 to 27 mm for positrons.

Figure 5.10.b presents the mean shower radius for the Monte Carlo for the different beam energies. It is systematically smaller than the data by an average of 9%.

6 Hadrons

This chapter discusses the analysis of the data of pions and protons. First, the event selection is described in section 6.1. The subsequent sections present the energy distributions, the detector response, and the energy resolution. Results of two shower shape variables, the longitudinal profile and the mean shower radius, are then presented. The chapter concludes with the comparison of the data with the Monte Carlo in section 6.7.

6.1. Event selection

The Cherenkov counters are used as a first selection for pions and protons in data. There is irreducible muon contamination due to in-flight pion decays to muons. The procedure to reject muons and noise is explained for pions, but is also applied for protons.

Events are rejected on the basis of two variables: number of hits and k_{COG} (Eq. 5.1). Figure 6.1 shows the number of events depending on the number of hits and k_{COG} for the energies 3 GeV and 10 GeV for pions. Muon events are concentrated at the peak at ($k_{\mathrm{COG}} = 15, \mathrm{hits} = 38$). Pion events show a large spread. For low momenta ($p \leq 5\,\mathrm{GeV}$), muons overlap pions (Figure 6.1.a) while for higher momenta ($p > 5\,\mathrm{GeV}$) the two are clearly separated (Figure 6.1.b). Events in the green solid box are rejected. Events with a low number of hits (below the red dashed line) are considered to be noise and are also rejected.

To recover possible pions among the rejected events, those with a shower are accepted. Showers are identified with the Primary Track Finder (PTF) algorithm [25].

Only the data in the beam momentum range 3 to 10 GeV are used for the analysis. The contamination of muons in the data for $p = 1\,\mathrm{GeV}$ and $p = 2\,\mathrm{GeV}$ can not be rejected (using the method described in this section) without creating a bias in the sample.

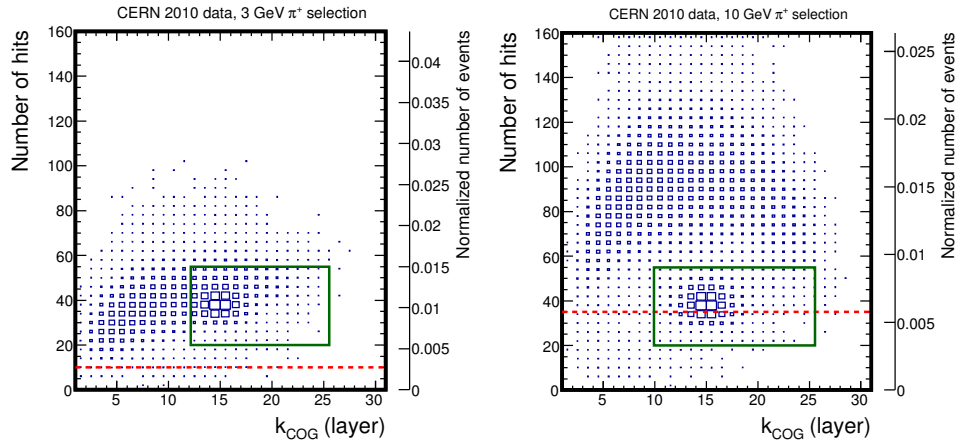

(a) (b)

Figure 6.1.: The number of hits against k_{COG} (Eq. 5.1) for 3 GeV (a) and 10 GeV (b) data events, selected as pions using Cherenkov counter information. Events inside the green box and below the red dashed line are rejected, unless a shower is detected.

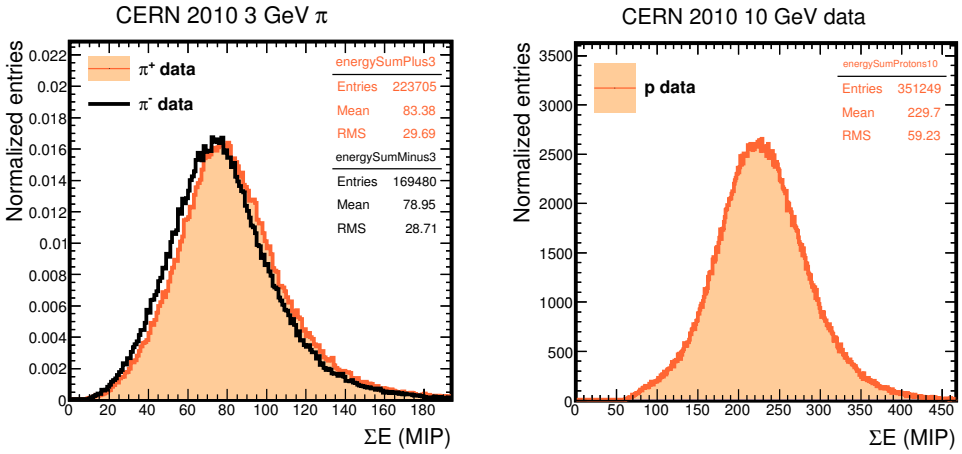

(a) (b)

Figure 6.2.: Energy sum distributions for 3 GeV pions (a) and 10 GeV protons (b).

6.2. Energy distribution

The energy sum distributions for both pions and protons are not Gaussian. Examples are shown in Figure 6.2 for 3 GeV pions (a) and 10 GeV protons (b). The shift between 3 GeV π^+ and π^- cannot be explained by the systematic uncertainty of the temperature correction.

The bias at the left side (for example the shoulder between 60 MIPs and 140 MIPs in Figure 6.2.b) is suspected to be due to multi-particle events with muons.

Table 6.1.: The available energy for pions and protons at different beam momenta.

	Available energy (GeV)		
Beam momentum (GeV)	Electrons	Pions	Protons
3	3.000	3.003	2.205
4	4.000	4.002	3.170
5	5.000	5.002	4.149
6	6.000	6.002	5.135
7	7.000	7.001	6.124
8	8.000	8.001	7.117
9	9.000	9.001	8.111
10	10.000	10.001	9.106

Table 6.2.: The detector response (Figure 6.3) is fitted with $E_{\text{reco}} = a \cdot E_{\text{available}} + b$ and the fitted values for the parameters are listed here.

parameter	π^+	π^-	p
a	24.25 ± 0.01	24.64 ± 0.01	23.93 ± 0.02
b	9.91 ± 0.08	4.59 ± 0.09	12.40 ± 0.11

6.3. Detector response

The detector response depends on the available energy of the particle. This is different for pions and protons. The available energy for pions can be expressed as

$$E_{\text{available}} = \sqrt{p^2 + m_{\pi^\pm}^2} \tag{6.1}$$

while for protons it is

$$E_{\text{available}} = \sqrt{p^2 + m_{\text{p}}^2} - m_{\text{p}} \tag{6.2}$$

where p is the momentum, $m_{\pi^\pm} = 139.57\,\text{MeV}$ the pion mass and $m_{\text{p}} = 938.27\,\text{MeV}$ the proton mass [1]. For different momenta, the available energies for pions and protons are shown in Table 6.1. The physical reason for the difference between $E_{\text{available}}$ for pions and protons is that protons do not decay, and thus the rest mass energy has to be subtracted from the total energy.

The detector response for pions and protons as a function of the available energy is presented in Figure 6.3.a. The reconstructed energy is given by the mean from the energy sum distribution (section 6.2). The red line is a fit of the proton data with the function $E_{\text{reco}} = a \cdot E_{\text{available}} + b$ in the range $2.205 \leq E_{\text{available}} \leq 9.106\,\text{GeV}$. The red dashed line is an extension of the fitted function to $E_{\text{available}} = 10\,\text{GeV}$. Values of the fit for protons as well as pions are summarized in Table 6.2.

The response for hadrons is in general non-linear, however, in the energy range of our data the response is observed to be linear. The deviation from the proton linearity is within 3% for both protons and π^+ (Figure 6.3.b). The response to π^- is systematically less than the response to its positive counterpart. It is expected to be the same, further study is thus required.

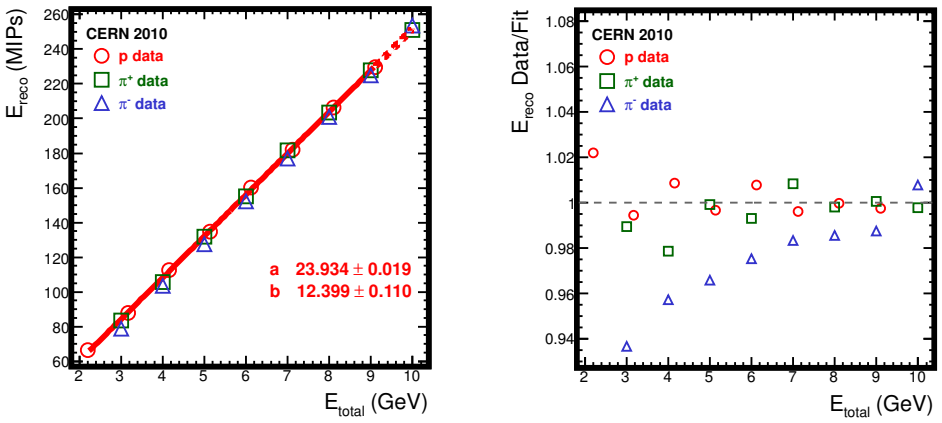

(a) (b)

Figure 6.3.: (a) The detector response versus the energy for protons (red circles), π^+ (green squares), and π^- (blue triangles). (b) The ratio of data and the proton linearity.

The response for 5 GeV electrons, 5 GeV pions and 5.1 GeV protons is shown in Figure 6.4.a. The energy of the pion data does not match that of the proton data exactly; the two closest energy points are chosen e.g. 5.002 GeV pions and 5.135 GeV protons. The dependence of the ratio between the pion and proton response on the energy is shown in Figure 6.4.b. Similarly, the two closest energy points are chosen for the pion/proton ratio. The red dashed line is the ratio of the available energies between pions and protons calculated from Eq. 6.1 and Eq. 6.2.

It follows from Figure 6.4.b that the pion response is smaller than the proton response between 3 GeV and 9 GeV. The opposite has however been predicted [26] and experimentally confirmed [27] for a non-compensating calorimeter for $E > 200\,\text{GeV}$. Similar opposite result has been observed for the ATLAS Tile calorimeter for energies between 50 GeV and 180 GeV [28].

The π/e^- ratio is shown in Figure 6.4.c for the tungsten detector while the ratio for the Fe-AHCAL [23] is shown in Figure 6.4.d. In the energy range of 3 GeV and 6 GeV, the W-AHCAL is within 6% of a compensating calorimeter ($\pi/e^- = 1$).

6.4. Energy resolution

The resolution for hadrons are shown in Figure 6.5 . For each energy, it is estimated as the mean divided by the RMS of the energy sum distribution (section 6.2). The data are fitted with Eq. 2.3 for pions in (a) and for protons in (b). The fitted values are summarized in Table 6.3. The increasing difference of the resolution between π^+ and π^- for $E \geq 6\,\text{GeV}$ is suspected to be due to multi-particle events as discussed in section 6.2.

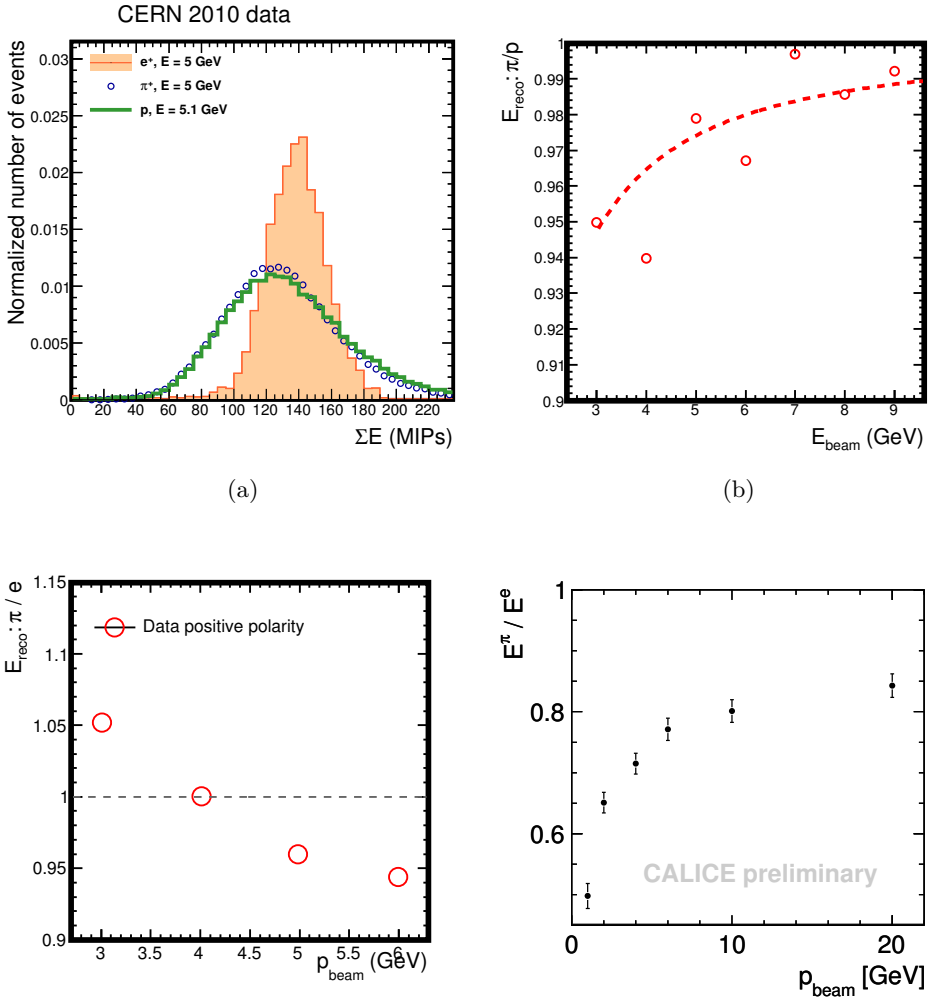

Figure 6.4.: (a) The energy sum distribution for 5 GeV e^+, 5 GeV π^+ and 5.1 GeV protons. (b) The ratio of the reconstructed energy for π/p. (c) The ratio of the reconstructed energy for π/e^+. (d) The π/e^+ ratio for the Fe-AHCAL [23].

6.5. Longitudinal profile

Examples for the longitudinal profile after the shower start are shown in Figure 6.6 for pions at 3 GeV and 10 GeV. The start of the shower is determined by using the Primary Track Finder (PTF) algorithm [25]. The distribution is similar for protons. A shower rise is expected in the first few layers; instead, there is a peak in the first layer. It is suspected that the shower start finder PTF does not work efficiently for energies below 10 GeV. The Monte Carlo shows similar results.

6.6. Mean shower radius

The mean shower radius (Eq. 5.7) is shown in Figure 6.7 as a function of the energy for protons (red circles), π^+ (green squares) and π^- (blue triangles). The results

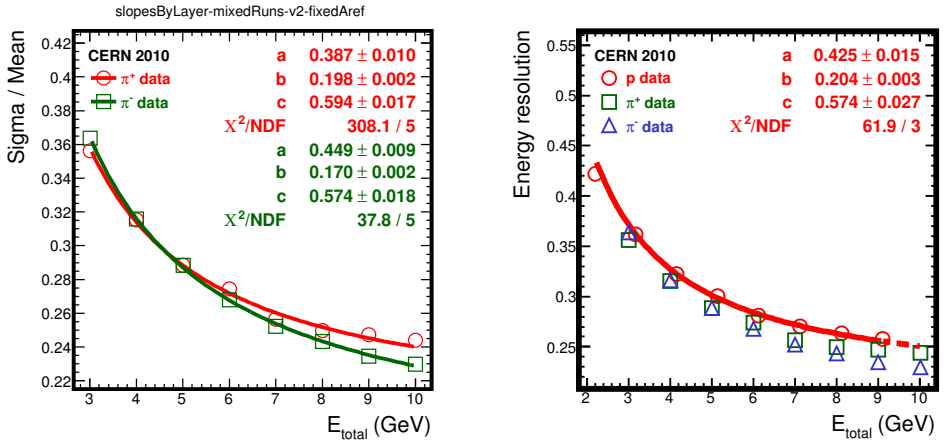

(a) (b)

Figure 6.5.: Energy resolution for pions (a) and protons (b). The solid line is the fit of the resolution with Eq. 2.3.

Table 6.3.: The energy resolution of the W-AHCAL for pions and protons

parameter	π^+	π^-	p
Stochastic term a (%GeV$^{1/2}$)	38.7 ± 1.0	44.9 ± 0.9	42.5 ± 1.5
Constant term b (%GeV)	19.8 ± 0.2	17.0 ± 0.2	20.4 ± 0.3
Noise term c (MeV)	594 ± 17	574 ± 18	574 ± 27

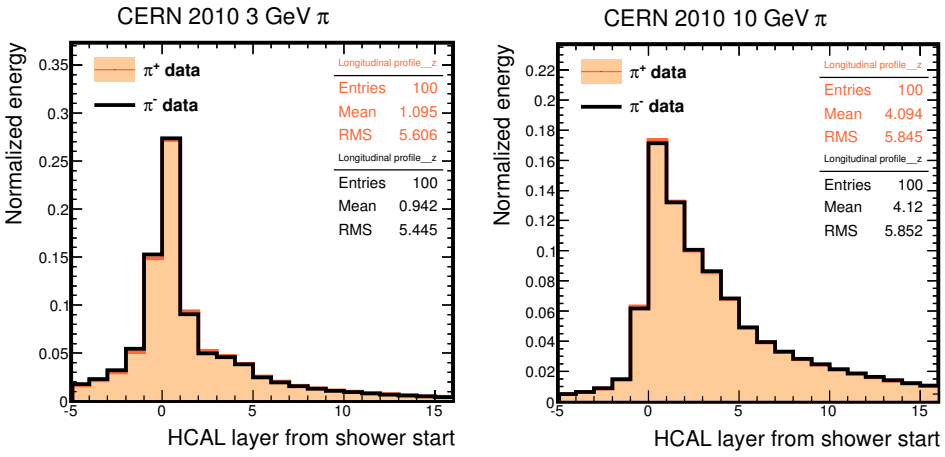

(a) (b)

Figure 6.6.: Longitudinal profile for 3 GeV (a) and 10 GeV (b) pions.

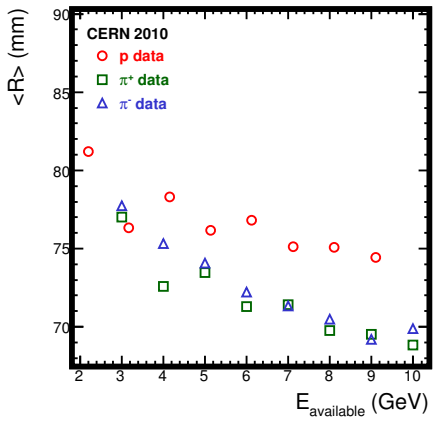

Figure 6.7.: The mean shower radius (Eq. 5.7) is plotted versus the beam energy for protons (red circles), π^+ (green squares), and π^- (blue triangles).

for the pions should be consistent, but at $E = 4\,\text{GeV}$ there is a difference. This discrepancy is not yet understood. A future study would involve comparing the beam profiles, spatial hit distributions, and the energy hit spectra between 4 GeV π^+ and π^-. Since the proton and π^+ events are selected from the same runs, understanding this discrepancy would consequently also mean understanding the proton data point at 3.170 GeV.

6.7. Comparison with Monte Carlo

In this section, the response, the energy resolution and the mean shower radius are compared with Monte Carlo simulations. Three physics lists are taken into account: QGSP_BERT_HP, FTFP_BERT_HP and QGSP_BIC_HP. The Monte Carlo results for π^+ and π^- are similar, only comparisons for π^+ and protons with Monte Carlo are therefore shown.

The physics list QGSP_BIC_HP should not be used for pions below 25 GeV. It is included in this analysis for completeness only. The reason is that QGSP_BIC_HP uses LEP for the pions for energies between 0 GeV and 25 GeV. For protons however, BIC is used between 0 GeV and 9.9 GeV.

The Bertini-cascade-family physics lists use the same model between 0 and 4 GeV (Figure 4.2). Identical results are thus expected in that energy range. As it will be shown, this is not the case. The difference is due to the usage of different versions of GEANT4: version 9.3.p2 for QGSP_BERT_HP while version 9.4.p3 is used for both FTFP_BERT_HP and QGSP_BIC_HP.

Figure 6.8 shows the comparison of the data with the Monte Carlo for the π^+ (a) and proton (b) response. Both QGSB_BERT_HP and FTFP_BERT_HP have an increased response of up to 4%. The binary cascade shows the opposite behavior. The decrease for the protons is up to 5% and for the pions it is up to 13%.

The comparison of the resolution in the Monte Carlo with the data is shown in Figure 6.9. The physics lists stay within 8% of the data except for QGSP_BIC_HP for the pions. In the energy range of 3 GeV and 5 GeV the difference is up to 28%.

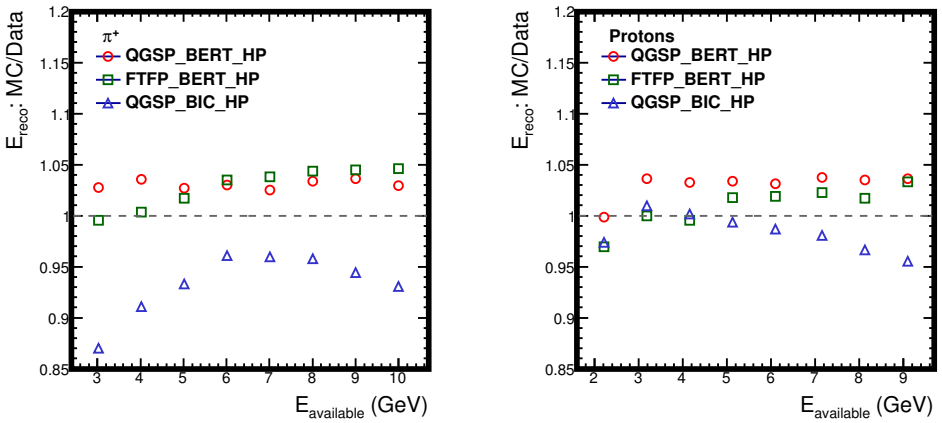

(a) (b)

Figure 6.8.: Ratio of the reconstructed energy in the Monte Carlo and in the data for π^+ (a) and protons (b).

The mean shower radius for all energies is compared to the three physics lists in Figure 6.10. The binary cascade model underestimates the data between 7% and 12% for both the pions and protons. The QGSP_BERT_HP list on the other hand overestimates it between 2% and 6%. The Fritiof model is within 3% of the data for the protons and within 8% for the pions.

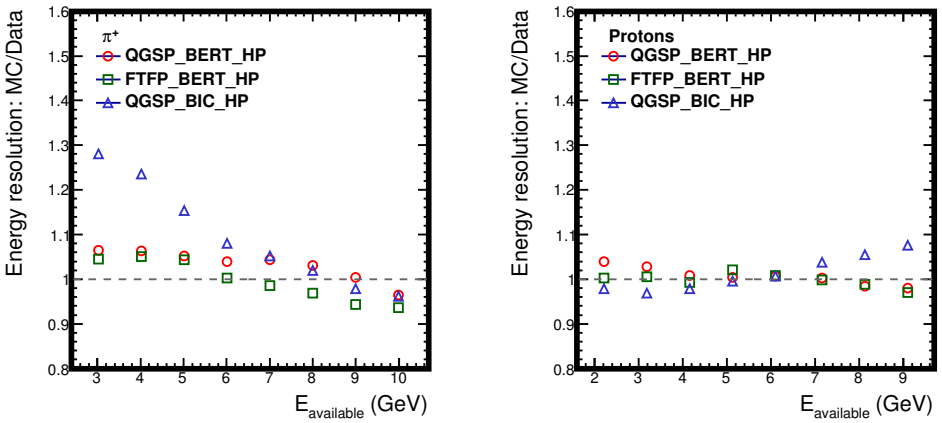

(a) (b)

Figure 6.9.: Ratio of the energy resolution in the Monte Carlo and in the data for π^+ (a) and protons (b)

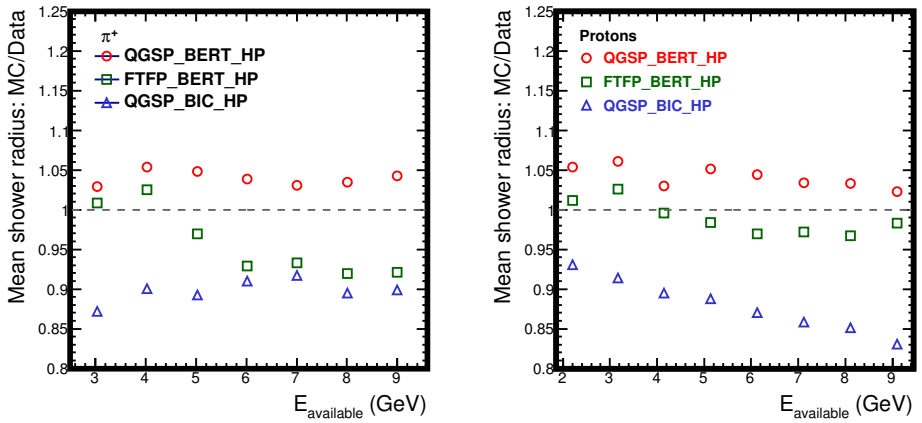

(a) (b)

Figure 6.10.: Ratio of the mean shower radius in the Monte Carlo and in the data for π^+ (a) and protons (b)

7
Summary & Outlook

A highly granular analogue hadron calorimeter was developed for a future linear electron-positron collider. Test beam data was recorded with tungsten as the absorber material at CERN in 2010 and 2011. This work presents the analysis of the data taken in 2010. This analysis provides data for the validation of hadronic simulation models for tungsten, including the shower shapes. In addition, the energy resolution is measured for electrons, pions and protons and compared with the performance of other calorimeters.

The electron and positron data cover the range from 1 GeV to 6 GeV. The hadron data (π^+, π^-, p) cover the beam momentum range 3 GeV to 10 GeV. The data quality for the hadron data is not yet fully validated. The stated numbers for the hadrons are therefore preliminary.

The energy resolution has three contributions: the stochastic term, the constant term and the noise term. The values are presented in Table 7.1. The electromagnetic resolution is worse than for the Fe-AHCAL [23]. This is expected due to the shorter radiation length of tungsten. The difference between the noise term obtained via the fit and via analysis of the noise events is not yet understood and requires further study. The analysis on pion and proton energy resolution requires further work on improving the purity of the data.

Table 7.1.: The energy resolution of W-AHCAL where a is the stochastic term and b the constant term. The noise term c for e^+/e^- is determined in two ways (section 5.4): from the fit and from noise events.

Parameters	e^+	e^-	π^+	π^-	p
a ($\%/\sqrt{E\,(\mathrm{GeV})}$)	28.7 ± 0.1	27.9 ± 0.1	38.7 ± 1.0	44.9 ± 0.9	42.5 ± 1.5
b ($\%/E\,(\mathrm{GeV})$)	0.0 ± 3.6	0.0 ± 3.6	19.8 ± 0.2	17.0 ± 0.2	20.4 ± 0.3
c (MeV), fit	190 ± 4	202 ± 3	594 ± 17	574 ± 18	574 ± 27
c (MeV), noise	53	56			

The mean shower radius has a maximum value of 62 mm at 1 GeV and decreases to 26 mm at 6 GeV. The mean shower radius for protons is between 74 mm and 81 mm, while for the pions they are between 69 mm and 78 mm.

The shower maximum $t_{\max}$ for both electrons and positrons is between 3.9 X_0 and 5.6 X_0. The longitudinal profile for the hadrons from the first hard interaction suggests that the algorithm to find the shower start does not work properly for momenta below 10 GeV. Further study is required to determine the shower start for low-momentum hadrons.

Three physics lists were used to validate the hadron interactions in tungsten: QGSP_BERT_HP, FTFP_BERT_HP and QGSP_BIC_HP. In general the Monte Carlo is within 8% agreement with the data.

The physics list QGSP_BIC_HP uses different simulation models for pions and protons for $E_{\text{kinetic}} \leq 9.9\,\text{GeV}$. For pions the LEP model is used. It shows significant deviations with the data, but this was expected. For protons the BIC model is used and is within 8% agreement with the data. However, the mean shower radius has significant deviations compared to the data.

A
Run list

Table A.1.: Run list for positive polarity. The temperature is the average temperature of the calorimeter. The pressures of the Cherenkov counters are in bar absolute.

p (GeV)	Run nr.	Nr. of events	T (°C)	Cher-A (bar)	Cher-B (bar)
1	360628	47012	24.1	0.3	0.3
1	360629	47518	24.2	0.2	0.2
1	360630	47152	24.7	0.7	0.7
2	360550	93162	21.2	1.0	3.02
2	360551	98169	21.2	1.0	3.02
2	360552	93134	21.2	1.0	3.02
2	360573	144106	21.4	1.0	3.04
2	360810	138721	20.3	1.0	3.04
2	360811	139598	20.4	1.0	3.04
3	360598	144280	23.4	1.01	3.01
3	360599	141844	23.5	1.01	3.01
3	360615	139806	24.7	1	3
3	360616	140618	24.6	1	3
4	360536	143674	20.4	0.60	3.01
4	360543	114622	20.2	0.60	3.02
4	360570	145181	20.9	0.6	3.02
4	360571	141134	21.0	0.60	3.02
4	360801	133114	20.9	0.60	3.05
4	360802	132928	20.6	0.6	3
5	360591	140628	23.2	0.3	3
5	360597	141814	23.3	0.3	3.01
5	360613	140177	24.7	0.40	3.02
5	360614	140071	24.7	0.40	3.02

Table A.1.: Run list for positive polarity. The temperature is the average temperature of the calorimeter. The pressures of the Cherenkov counters are in bar absolute.

p (GeV)	Run nr.	Nr. of events	T (°C)	Cher-A (bar)	Cher-B (bar)
6	360533	143813	20.9	0.2	3.02
6	360534	142042	20.7	0.2	3.02
6	360563	142554	20.6	0.2	3.0
6	360564	146689	20.7	0.20	3.02
6	360617	139661	24.4	0.3	3
6	360618	140214	24.3	0.3	3
6	360799	132870	21.6	0.35	3
6	360800	132692	21.3	0.35	3
7	360589	140836	20.7	0.15	3
7	360590	141064	23.2	0.15	3
7	360611	141449	24.5	0.23	3.02
7	360612	140840	24.6	0.23	3.02
7	360644	141272	25.8	0.3	3
7	360645	141293	25.7	0.3	3.0
8	360532	141670	21.0	0.1	3.02
8	360561	141011	20.5	0.1	3.0
8	360626	140305	23.9	0.15	3.0
8	360627	142415	23.9	0.2	3.0
8	360633	139586	25.2	0.2	3.0
8	360796	132215	22.4	0.25	3
8	360797	90706	22.1	0.35	3.0
8	360619	140555	24.1	0.15	3
9	360642	141267	25.8	0.21	3.0
9	360643	140872	25.8	0.2	3.0
9	360837	139935	20.7	0.2	3.0
9	360838	140446	20.8	0.2	3.0
10	360640	141262	25.6	0.2	3.0
10	360641	139721	25.7	0.2	3.0
10	360786	130943	21.4	0.2	3.06
10	360795	121204	22.4	0.2	3.0

Table A.2.: Run list for negative polarity. The temperature is the average temperature of the calorimeter. The pressures of the Cherenkov counters are in bar absolute.

p (GeV)	Run nr.	Nr. of events	T (°C)	Cher-A (bar)	Cher-B (bar)
−1	360583	141715	22.5	0.50	0.49
−1	360584	125418	22.6	0.10	0.10
−2	360782	92312	20.7	0.99	3.0
−2	360785	139578	20.8	0.99	3.0
−3	360835	139580	20.6	1.0	3.0

Table A.2.: Run list for negative polarity. The temperature is the average temperature of the calorimeter. The pressures of the Cherenkov counters are in bar absolute.

p (GeV)	Run nr.	Nr. of events	T (°C)	Cher-A (bar)	Cher-B (bar)
−3	360836	154270	20.6	1.0	3.0
−4	360774	140868	20.9	0.59	3
−5	360827	139757	20.8	0.40	3.00
−5	360834	135507	20.6	0.4	3.0
−6	360707	127755	20.3	0.35	3.0
−6	360771	138711	21.3	0.36	3
−6	360772	139620	21.2	0.36	3
−7	360825	148549	20.9	0.30	3.00
−7	360826	129739	20.9	0.30	3.00
−8	360767	130632	21.8	0.25	3.0
−8	360770	137279	21.6	0.25	3
−9	360823	139478	21.0	0.21	2.99
−9	360824	139287	21.0	0.21	2.99
−10	360646	129504	25.6	0.2	0.2
−10	360647	120134	25.6	0.2	0.2

Bibliography

[1] K. Nakamura et al. The review of particle physics. *J. Phys. G*, 37(7A):075021, 2010.

[2] Peter W. Higgs. Broken symmetries and the masses of gauge bosons. *Phys. Rev. Lett.*, 13:508–509, Oct 1964. doi: 10.1103/PhysRevLett.13.508. URL `http://link.aps.org/doi/10.1103/PhysRevLett.13.508`.

[3] G. Weiglein et al. Physics interplay of the LHC and the ILC. *Phys. Rep.*, 426: 47–358. 472 p, Oct 2004.

[4] International Linear Collider Reference Design Report. 1: Executive summary. 2: Physics at the ILC. 3: Accelerator. 4: Detectors, 2007. ILC-REPORT-2007-001.

[5] H. Schmickler, P. Lebrun, N. Toge, N. Phinney, T. Garvey, P. Burrows, M. Draper, and M. Aicheler, editors. *A Multi-TeV Linear Collider Based on CLIC technology: CLIC Conceptual Design Report.* CERN, 2012.

[6] M. A. Thomson. Particle Flow Calorimetry and the PandoraPFA Algorithm. *Nucl. Instrum. Meth.*, A611:25–40, 2009.

[7] Richard Wigmans. *Calorimetry - Energy Measurement in Particle Physics.* International Series of Monographs on Physics, volume 107. Oxford University Press, New York, 2000.

[8] PDG Atomic and nuclear properties of materials. Website: `http://pdg.lbl.gov/2011/AtomicNuclearProperties/`.

[9] F. Cavallari. Performance of calorimeters at the LHC. *Journal of Physics: Conference Series*, 293(1):012001, 2011.

[10] M. Livan. XIII International conference on calorimetry in high energy physics (CALOR 2008). *Journal of Physics: Conference Series*, 160(1):011001, 2009.

[11] CALICE collaboration. Shower development of 1 to 10 GeV particles in the CALICE scintillator-tungsten HCAL. *CALICE Analysis Notes*, CAN-036, 2012.

[12] S. Agostinelli et al. GEANT4– A Simulation Toolkit. *Nucl. Instrum. Meth.*, A506(3):250–303, July 2003.

[13] A. Münnich. Status of analysis for WHCAL test beam at CERN. Talk at `http://ilcdoc.linearcollider.org/record/31162`.

[14] G. Bondarenko et al. Limited Geiger-mode microcell silicon photodiode: new results. *Nucl. Instrum. Meth.*, A442(1–3):187–192, 2000.

[15] A. Kaplan. *Hadronic imaging calorimetry.* PhD thesis, Universität Heidelberg, 2011.

[16] N. Feege. *Silicon photomultipliers: properties and application in a highly granular calorimeter.* PhD thesis, Universität Hamburg, 2008.

[17] C. Grefe. MIP calibration for CERN2010 data. Talk at `http://indico.cern.ch/contributionDisplay.py?contribId=0&confId=133403`.

[18] D. Dannheim, W. Klempt, and A. Lucaci-Timoce. Update on particle ID for W-HCAL testbeam analysis. Talk at `http://indico.cern.ch/getFile.py/access?contribId=5&resId=0&materialId=slides&confId=118843`.

[19] B. Lenzi. Particle identification with Cherenkov counters and W-HCAL. Talk at `http://indico.cern.ch/getFile.py/access?contribId=1&resId=1&materialId=slides&confId=128871`.

[20] GEANT4 model/process catalog. Website: `http://geant4.cern.ch/support/proc_mod_catalog/models/`.

[21] S. Richter. *Validation of the calibration procedure for a highly granular calorimeter with electromagnetic processes.* PhD thesis, Universität Hamburg, 2008.

[22] CALICE collaboration. Electromagnetic response of a highly granular hadronic calorimeter. *JINST*, 6(04):P04003, 2011.

[23] CALICE collaboration. Analysis of low energetic electron and pion data collected with the AHCAL prototype at Fermilab. *CALICE Analysis Notes*, CAN-034, 2011.

[24] C. Leroy and P. Rancoita. Physics of cascading shower generation and propagation in matter: principles of high-energy, ultrahigh-energy and compensating calorimetry. *Reports on Progress in Physics*, 63(4):505, 2000.

[25] CALICE collaboration. Pion showers in the CALICE AHCAL. *CALICE Analysis Notes*, CAN-026, 2011.

[26] T.A. Gabriel et al. Energy dependence of hadronic activity. *Nucl. Instrum. Meth.*, A338(2–3):336–347, 1994.

[27] N. Akchurin et al. On the differences between high-energy proton and pion showers and their signals in a non-compensating calorimeter. *Nucl. Instrum. Meth.*, A408(2–3):380–396, 1998.

[28] P. Adragna et al. Measurement of pion and proton response and longitudinal shower profiles up to 20 nuclear interaction lengths with the ATLAS Tile calorimeter. *Nucl. Instrum. Meth.*, A615(2):158–181, 2010.